

Characterization of Few-Layer 1T' MoTe₂ by Polarization-Resolved Second Harmonic Generation and Raman Scattering

Ryan Beams,[†] Luiz Gustavo Cançado,[‡] Sergiy Krylyuk,^{†,||} Irina Kalish,[†] Berç Kalanyan,[†] Arunima K. Singh,[†] Kamal Choudhary,[†] Alina Bruma,[†] Patrick M. Vora,[§] Francesca Tavazza,[†] Albert V. Davydov,[†] and Stephan J. Stranick^{*,†}

[†]Material Measurement Laboratory, National Institute of Standards and Technology, Gaithersburg, Maryland 20899, United States

[‡]Departamento de Física, Universidade Federal de Minas Gerais, Belo Horizonte, Minas Gerais 30123-970, Brazil

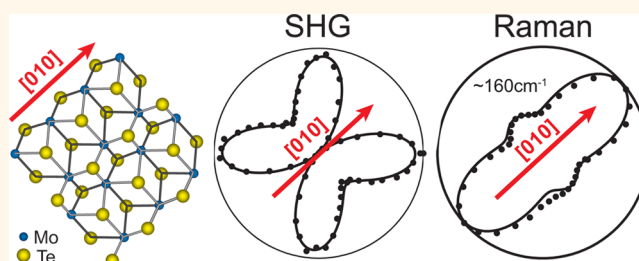
^{||}Theiss Research, La Jolla, California 92037, United States

[§]Department of Physics and Astronomy, George Mason University, Fairfax, Virginia 22030, United States

S Supporting Information

ABSTRACT: We study the crystal symmetry of few-layer 1T' MoTe₂ using the polarization dependence of the second harmonic generation (SHG) and Raman scattering. Bulk 1T' MoTe₂ is known to be inversion symmetric; however, we find that the inversion symmetry is broken for finite crystals with even numbers of layers, resulting in strong SHG comparable to other transition-metal dichalcogenides. Group theory analysis of the polarization dependence of the Raman signals allows for the definitive assignment of all the Raman modes in 1T' MoTe₂, and clears up a discrepancy in the literature. The Raman results were also compared with density functional theory simulations and are in excellent agreement with the layer-dependent variations of the Raman modes. The experimental measurements also determine the relationship between the crystal axes and the polarization dependence of the SHG and Raman scattering, which now allows the anisotropy of polarized SHG or Raman signal to independently determine the crystal orientation.

KEYWORDS: two-dimensional material, Raman scattering, second harmonic generation, crystal symmetry, optical spectroscopy



The experimental realization of two-dimensional crystals has led to a new era of low-dimensional materials research. In conjunction with graphene and boron nitride, transition-metal dichalcogenides (TMDs) are actively being pursued for applications such as photovoltaics, flexible electronics, and chemical sensors.¹ While most of the research on TMDs has emphasized crystals with semiconducting behavior,² semimetallic TMDs have been shown to have large magnetoresistances³ and superconductivity⁴ as well as promising quantum spin Hall and Weyl semimetal properties.^{5–8} One such example is molybdenum ditelluride (MoTe₂), which can be converted between semiconducting hexagonal phase (2H or α -MoTe₂) and semimetallic monoclinic phase (1T' or β -MoTe₂) polymorphs. MoTe₂ exhibits large spin–orbit coupling and a near-infrared bandgap for 2H phase and strong magnetic properties for 1T' phase.^{9–11} Additionally at temperatures below ≈ 250 K, 1T' converts to a semimetallic orthorhombic phase known as T_d ^{12–14} that shows promise as a Weyl semimetal,⁸ which has been experimentally demonstrated in MoTe₂, WTe₂, and MoWTe₂.^{15–24} Studying the crystal phase

1T' is relevant for a broader range of materials, such as ReS₂ and ReSe₂, which exhibit semiconductor properties with weak interlayer coupling.^{25,26}

The unique properties of 1T' MoTe₂ derive from the underlying crystal symmetry. Optical techniques, such as second harmonic generation (SHG)^{27–33} and Raman scattering,^{34–36} provide nondestructive means to probe the symmetries of two-dimensional materials. Due to the sensitivity of nonlinear optical processes to crystal symmetry, SHG allows for optical determination of the crystal orientation and symmetry of a crystal on a substrate. Since 1T' is symmetric under inversion, no SHG is expected. However, as has been shown for other TMDs, the crystal symmetry can change for odd compared to even numbers of layers.^{27–29} Similarly, the active Raman modes also depend on the crystal symmetry.^{26,37–41} While the Raman properties of the 2H phase have

Received: July 30, 2016

Accepted: October 5, 2016

Published: October 5, 2016

been extensively studied,^{10,42,43} the 1T' phase has not been fully characterized, and there is significant discrepancy in the literature on the Raman modes assignment as well as the number of modes observed.^{13,44–50}

We investigate the crystal symmetry of 1T' MoTe₂ by measuring the polarization dependence of the SHG and Raman scattering. The bulk material is known to be monoclinic, belonging to the nonsymmorphic space group $P2_1/m$ (C_{2h}^2 in Schönflies notation, or #11 in the International Tables for Crystallography, Vol. A⁵¹).^{12,52} However, the dependence of the crystal symmetry on the number of layers (N) has not been studied for 1T' MoTe₂. We find that the inversion symmetry is broken for even numbers of layers, leading to a strong SHG signal. The polarization dependence shows that samples with even layers are still monoclinic as expected for the 1T' phase, but with symmetry defined by the symmorphic space group Pm (C_s^1 , #6).⁵¹ Similar behavior is expected for other crystals with 1T' phase, such as ReS₂ and ReSe₂.²⁶ The wavelength and layer dependence of nonlinear susceptibility was measured, and the magnitude is comparable to other TMDs. We further characterized the optical properties of few-layer crystals with even and odd layers by assigning each Raman mode based on the polarization dependence. In addition, the imaginary parts of the complex components of the Raman tensors are required to explain the polarization dependence, which indicates that optical absorption in this material is significant. The polarization dependence also revealed that the totally symmetric Raman mode at ≈ 260 cm⁻¹ is comprised of at least two peaks, although some simulations predict additional peaks.^{44,49} These measurements help to clarify a discrepancy in the literature concerning the Raman scattering from 1T' MoTe₂ as well as illustrate the changes in the crystal symmetry with layer parity. Finally, we demonstrate the relationship between the crystal axes and Raman polarization dependence, thereby enabling the identification of crystal orientation from Raman measurements alone.

RESULTS AND DISCUSSION

Bulk 1T' MoTe₂ belongs to the C_{2h}^2 ($P2_1/m$, #11) non-symmorphic monoclinic space group.^{12,52} The symmetry operations associated with this group are the identity E , a two-fold $C_{2y}(0,1/2,0)$ screw axis along the y direction (as defined in Figure 1a), a horizontal mirror σ_{xz} , and the inversion i . These symmetry elements are illustrated in Figure 1a, showing the top view of the crystal structure of monolayer 1T' MoTe₂. The same symmetry operations hold for any sample with an odd number of layers, N , monolayer included. As such, they also belong to the C_{2h}^2 space group. However, the inversion symmetry is broken for 1T' MoTe₂ with even layers, and the two-fold screw rotation is also no longer applicable. Since the reflection operation is still preserved, all samples with even layers fit into the C_s^1 (Pm , #6) space group. The breakdown of inversion symmetry for an even number of layers is seen from the side view of the crystal structure depicted in Figure 1b.

As discussed above, SHG is an excellent tool to characterize the presence or absence of inversion symmetry. Furthermore, crystal symmetry plays an important role in Raman spectroscopy. To study the symmetry properties of 1T' MoTe₂ using these techniques, crystalline platelets were grown using an iodine-assisted chemical vapor transport (CVT) method and subsequently exfoliated onto an SiO₂/Si substrate. Figure 1c shows a light microscope image of the MoTe₂ sample with the various number of layers labeled, which were determined by

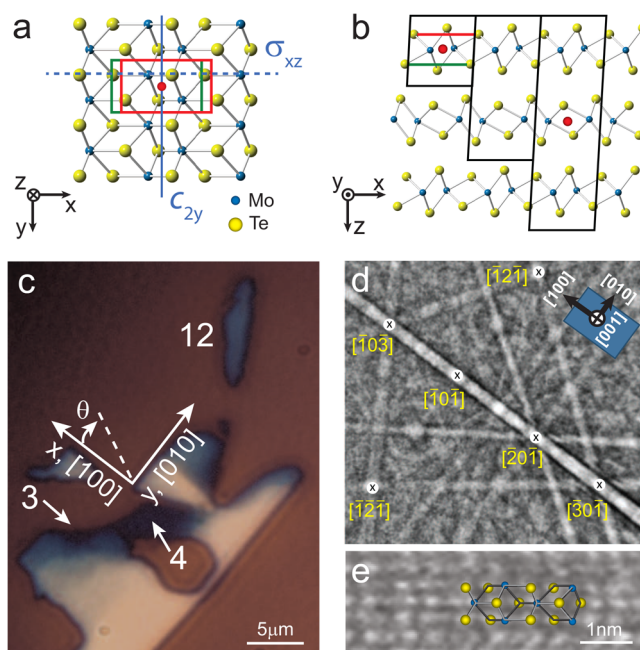


Figure 1. (a) Top view of crystal structure of monolayer 1T' MoTe₂. The green and red rectangles show two cuts of the unit cell parallel to the layer plane. The red dots indicate the center of inversion symmetry, the solid line indicates the $C_{2y}(0,1/2,0)$ screw axis, and the dashed line indicates the horizontal mirror plane σ_{xz} . (b) Side view of the crystal structure for monolayer ($N = 1$), bilayer ($N = 2$), and trilayer ($N = 3$) lattices. The red circles in the center of the $N = 1$ and 3 unit cells indicate inversion symmetry centers as well as $C_{2y}(0,1/2,0)$ screw axes perpendicular to the figure plane (along the y direction). The green and red lines are the projections of the respective rectangles in (a). (c) Light microscope image of MoTe₂ sample. The crystal orientation and regions with $N = 3$, 4, and 12 are indicated. The white dashed line indicates the polarization direction at an angle, θ , relative to the x -axis. (d) EBSD pattern from the flake in (a) with the Kikuchi lines indexed to the 1T' crystal structure. Inset: The corresponding unit cell with the crystallographic directions labeled. (e) HAADF-STEM image of 1T' MoTe₂. The intensity variations are attributed to the atomic number difference between Mo ($Z_{\text{Mo}} = 42$) and Te ($Z_{\text{Te}} = 52$).

atomic force microscopy (AFM). The direction (white dashed line) and rotation angle (θ) of the polarization relative to the x -axis are also indicated. The crystal axes, determined by electron backscatter diffraction (EBSD) and confirmed with SHG (Figure 1d), are also indicated. The phase and stoichiometry of the bulk material were confirmed with Raman spectroscopy, X-ray diffraction (XRD), X-ray photoelectron spectroscopy (XPS), and high-angle annular dark-field scanning transmission electron microscopy (HAADF-STEM). While the exfoliation process removed the surface oxides, some oxides were detected using XPS in the unexfoliated regions of the bulk material. Figure 1e shows the HAADF-STEM image of the 1T' MoTe₂ with the crystal diagram overlaid.

Topographic images acquired by an AFM of the $N = 3$, 4, and 12 regions of the sample are shown in Figures 2a,b, respectively. Thickness of the $N = 3$ and 4 regions was also confirmed using the relative amplitude of the strongest Raman peak (see Supporting Information). The SHG images of these two regions are shown in Figures 2c,d, respectively. The white lines in c and d represent the topographic outlines of the crystal (solid) and step edges (dashed). The SHG images were acquired using a 75 fs Ti:sapphire laser centered at 992 nm.

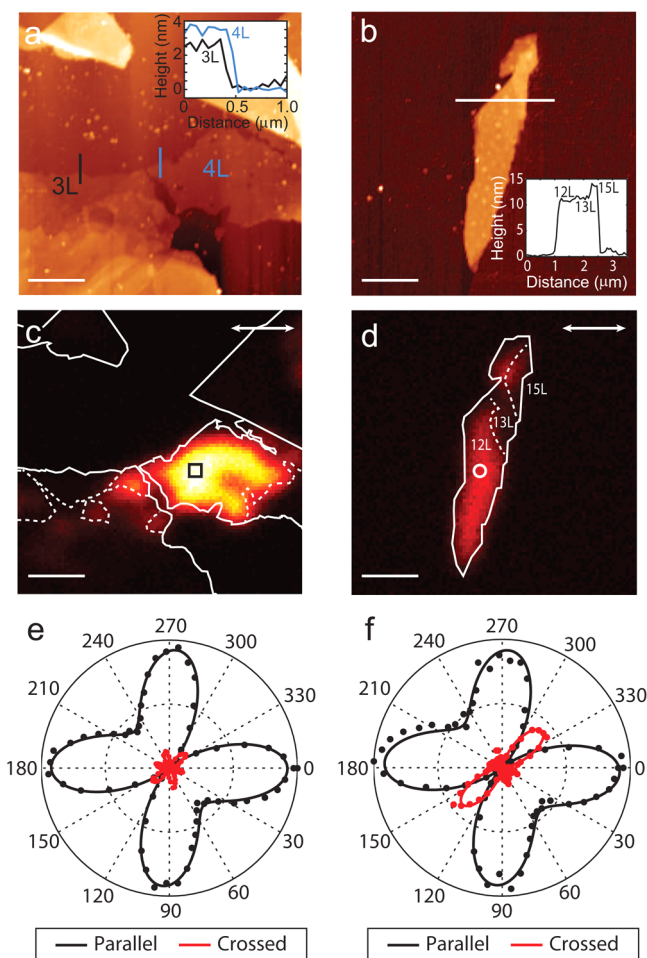


Figure 2. (a) Topography of the $N = 3$ and 4 regions of the sample. Inset: Linecuts along the blue and black lines. (b) Topography of the $N = 12$ region. (c, d) SHG images of the regions shown in (a) and (b), respectively. The crystal and step edges are shown as solid and dashed lines, respectively. Color contrast is scaled by $\times 2$ in (d). (e, f) SHG polar maps with the polarizer and analyzer parallel (black) and crossed (red) acquired at the black square ($N = 4$) in (c) white circle ($N = 12$) in (d), respectively. The angle is relative to the initial polarization (white double arrow in c and d) and in the direction defined in Figure 1c. Scale bar = $2 \mu\text{m}$.

The excitation wavelength was chosen to maximize the SHG signal and is nearly resonant with the electronic band structure at the Γ point.⁴⁸ While the signal may be stronger further into the infrared region, the wavelength was chosen to be at the far end of the Ti:sapphire gain curve. This image demonstrates that the trilayer ($N = 3$) and bulk (>25 layers) regions of the sample have no SHG signal. In contrast, the $N = 4$ region has a strong SHG signal, indicating broken inversion symmetry. In addition to the $N = 4$ region, a weaker SHG signal, by a factor 6, was observed from the $N = 12$ region in Figure 2d. The information contained in these images show that while bulk and $N = 3$ 1T' MoTe₂ are symmetric under inversion (as expected for any 1T' MoTe₂ sample with odd number of layers), the inversion symmetry is broken for even numbers of layers, as described in Figure 1.

To characterize the crystal symmetry and orientation of the sample, we measured the polarization dependence of the SHG signal. The SHG polarization dependence for the $N = 4$ region (black square in Figure 2c) and the $N = 12$ region (white circle

in Figure 2d) with the excitation polarization and analyzer parallel (black) and crossed (red) are shown in Figure 2e,f, respectively. Each plot was normalized by the maximum signal from the parallel data set, and the zero angle is relative to the incident polarization (white arrow in Figure 2b). There are several important contrasts to materials with a 2H phase TMDs that have previously been measured. First, the signal is significantly stronger when the polarizer and analyzer are parallel. This means that the orientation of the crystal with respect to the excitation polarization is critical to maximize the SHG intensity even in the absence of an analyzer, unlike 2H materials where the summed parallel and crossed SHG signal intensity is independent of excitation polarization.^{27–29} Second, the parity of the layer dependence is opposite of 2H materials, which are noninversion symmetric for monolayer and bulk.

Figures 3 and 4 show measurements from additional flakes to further explore the layer dependence of the SHG signal. Figure

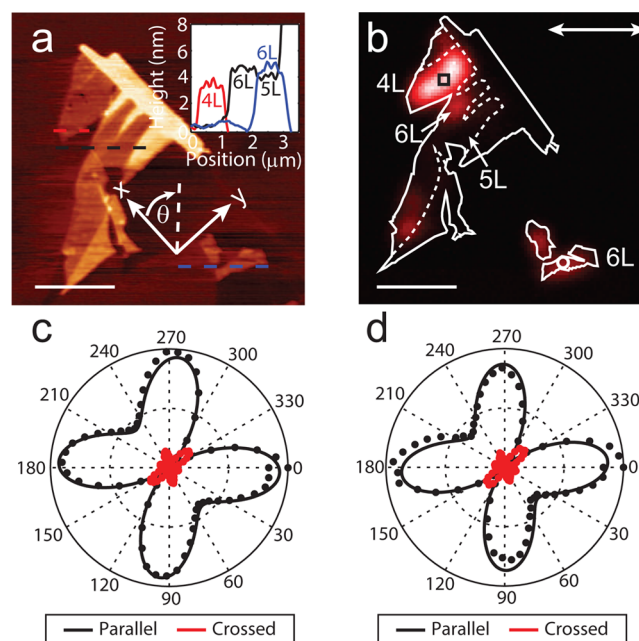


Figure 3. (a) Topography and (b) SHG images of another sample. (c, d) SHG polarization polar maps with the polarizer and analyzer parallel (black) and crossed (red) acquired at the black square ($N = 4$) and white circle ($N = 6$) in (b), respectively. The crystallographic axes are shown in (a). The angle in the polar plots is relative to the initial polarization, shown as a white double arrow (b). Scale bar = $3 \mu\text{m}$.

3a,b shows the topography and SHG images with the AFM cross sections shown in the inset. The polarization dependence of the $N = 4$ and 6 regions with the excitation polarization and analyzer parallel (black) and crossed (red) are shown in Figure 3c,d, respectively. As in Figure 2, each plot was normalized by the maximum signal from the parallel data set, and the zero angle is relative to the incident polarization (white arrow in Figure 3b). The correlation between the topography and the SHG image as well as the similarity in the polarization dependence with the results shown in Figure 2 provide additional evidence for layer-dependent inversion symmetry breaking. Figures 4a,b show white light images of additional larger crystals with the corresponding SHG images shown in Figures 4c,d. The insets show AFM linecuts along the black and blue dashed lines. In Figure 4c, the absence of any SHG signal

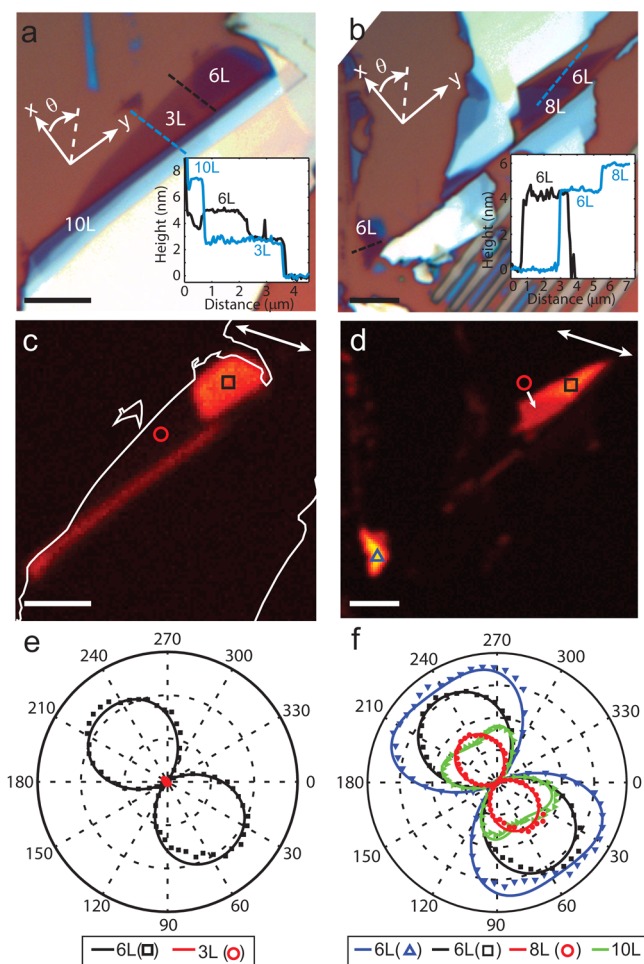


Figure 4. (a, b) White light images with the layer thicknesses and crystallographic axes labeled. Insets: AFM profiles along the black and blue dashed lines. (c, d) SHG images with the excitation polarization direction shown as a white arrow. Color contrast is scaled by $\times 2$ in (c) compared to (d). (e) SHG polarization polar map with the polarizer and analyzer parallel acquired at the black square ($N = 6$) and red circle ($N = 3$) in (c) are shown in black and red, respectively. (f) SHG polarization polar map with the polarizer and analyzer parallel acquired at the blue triangle ($N = 6$), the black square ($N = 6$), red circle ($N = 8$) in (d) and a nearby region ($N = 8$) are shown in blue, black, red, and green, respectively. The angle in the polar plots is relative to the horizontal axis in (b and c). Scale bar = $5 \mu\text{m}$.

combined with the bright 6L region provide an excellent illustration of the layer-dependent symmetry breaking. The polarization dependences of the 6L (black square) and 3L (red circle) regions were acquired in the parallel configuration and are shown in Figure 4e in black and red, respectively. These measurements determine the crystal orientation and verify the absence of SHG from the 3L region for all polarization directions. Figure 4f shows the polarization dependence acquired at three different locations in Figure 4d and an additional region in close proximity (see Supporting Information). The polarization dependence shows that the crystal orientation is the same for all regions. It is important to note that the polarization map shows that the SHG signals from the two 6L regions have similar maximum intensities despite the smaller sample (blue triangle) being brighter in Figure 4d. This intensity difference is due to the alignment of the

excitation polarization with the crystal axis. Therefore, SHG intensity images cannot be used to estimate crystal thickness without aligning the incident polarization to the crystal axis. It is also important to note the change in the shape of the polarization maps for the different regions. While in the parallel configuration all the samples have a defined two-lobe pattern and zero signal along the zigzag direction, the shape varies from circular to a butterfly pattern. The butterfly pattern appears on smaller flakes and is likely caused by strain effects from the substrate or the influence of the edges. Both patterns are consistent with a C_s crystal as will be discussed.

The polarization dependence of the SHG signal extracted from regions with even layers is understood by considering the nonlinear properties of the C_s point group. The incident electric field, $\hat{e}_{\omega}^2 = [E_x^2 \ E_y^2 \ E_z^2 \ 2E_yE_z \ 2E_xE_z \ 2E_xE_y] = [\cos^2\theta \ \sin^2\theta \ 0 \ 0 \ 0 \ 2\cos\theta \ \sin\theta]$, generates a second harmonic signal along the $\hat{e}_{2\omega} = [\cos\theta \ \sin\theta \ 0]$ and $\hat{e}_{2\omega} = [-\sin\theta \ \cos\theta \ 0]$ directions for parallel and crossed polarizations, respectively. The intensity of the SHG signal, I_{SHG} can be expressed as

$$I_{\text{SHG}} = |\hat{e}_{2\omega} \cdot \vec{d} \hat{e}_{\omega}^2|^2 \quad (1)$$

where \vec{d} is the second-order susceptibility tensor, $\chi^{(2)}$, in contracted notation.⁵³ For the C_s point group

$$\vec{d} = \begin{pmatrix} d_{11} & d_{12} & d_{13} & 0 & d_{15} & 0 \\ 0 & 0 & 0 & d_{24} & 0 & d_{26} \\ d_{31} & d_{32} & d_{33} & 0 & d_{35} & 0 \end{pmatrix} \quad (2)$$

Substituting eq 2 into eq 1 leads to

$$I_{C_s}^{\parallel} = |d_{11}\cos^3\theta + (d_{12} + 2d_{26})\cos\theta\sin^2\theta|^2 \quad (3)$$

$$I_{C_s}^{\perp} = |d_{12}\sin^3\theta + (d_{11} - 2d_{26})\cos^2\theta\sin\theta|^2 \quad (4)$$

where $I_{C_s}^{\parallel}$ and $I_{C_s}^{\perp}$ are the parallel and crossed polarized signals, respectively (see Methods section). Eqs 3 and 4 are used to fit the SHG polarization dependence (solid lines in Figures 2e,f, 3c,d, and 4e,f) and confirm that even-layer 1T' MoTe₂ belongs to the C_s point group. Unlike 2H materials, the various tensor elements do not have to be equal. According to eq 3, the SHG signal is minimized along the zigzag direction (y -axis in Figure 1) for the parallel polarization configuration, which is -43.2° and -42.4° in Figure 2c,d, respectively, as shown in Figure 1d. This slight difference in crystal axis is not surprising given that the two sample regions are not connected. For Figure 3, the SHG polar maps give a crystal orientation for the zigzag direction of -41.4° and -47.1° for the $N = 4$ and 6 regions, respectively, relative to the input polarization. In Figure 4e,f, the crystal orientations are -36.3° and -41.1° with respect to horizontal incident polarization, respectively.

These equations also help to explain the variations in the polarization maps. For example, due to the negative sign in the cross-polarized configuration, slight variations in tensor elements strongly affect the cross-polarized signal, as seen comparing the cross-polarized data between the $N = 4$ and 12 regions. In addition these equations explain the change between the two-lobe circular and butterfly polarization patterns. The polarization pattern is butterfly shaped when $d_{11} \leq d_{26}$ and a two-lobe circular pattern when $d_{11} > d_{26}$. Averaging the normalized coefficients from the polarization maps in Figures 2 and 3 gives $d_{11} = 0.65$, $d_{12} = 0.5$, and $d_{26} = 0.78$, while averaging the circular patterns in Figure 4 gives $d_{11} = 0.96$, $d_{12} = 0.44$, and

$d_{26} = 0.36$. Note that d_{12} remains approximately constant. The change in the polarization pattern can be thought of as a change in d_{26} , which originates from an incident field along the x and y axes, such as at 45° , and the SHG signal is along the y axis. While these two patterns do not correlate with the thickness of the crystal, smaller crystals do exhibit the butterfly pattern, which suggests that d_{26} is sensitive to strain from the substrate or edge effects. Based on these measurements, the polarization-dependent SHG signal provides a straightforward optical method for determining the crystallographic orientation for 1T' MoTe₂.

The surface second-order susceptibility, d_s , of 1T' MoTe₂ can be quantified by measuring reference samples under the same conditions. In this case, we measured monolayer MoS₂ prepared on the same substrate (see Supporting Information) and a 100 nm thick beta-barium borate (BBO) crystal. Using the wavelength dependence of d_s for MoS₂²⁸ gives a surface second-order susceptibility of $d_s = 1.0 \times 10^5 \text{ pm}^2/\text{V}$ at 992 nm for the $N = 4$ region in Figure 2. As a comparison, we also calibrated d_s of MoTe₂ using a 100 nm thick BBO crystal. Relative to the bulk crystal, d_s can be expressed as²⁷

$$d_s = \frac{\lambda}{2\pi} \frac{1}{[n(\omega) + n(2\omega)]} \sqrt{\frac{I_s}{I_{\text{BBO}}}} d_{22} \quad (5)$$

where I_s and I_{BBO} are the surface and reference BBO SHG intensities, respectively, and $n(\omega)$ and $n(2\omega)$ are the refractive indices of the reference material at the fundamental and second harmonic frequencies, respectively. This approach leads to $d_s = 9 \times 10^4 \text{ pm}^2/\text{V}$ for the 4L region, which is in good agreement with the calibration using monolayer MoS₂. Since the excitation wavelengths used are far off the resonance for BBO, the wavelength dependence of d_{22} for BBO can be calculated using the Miller rule,⁵³ which indicates that d_{22} for BBO is nearly wavelength independent since the refractive index is approximately constant. While our samples were prepared on SiO₂/Si, the cavity effect from this substrate has been shown to result in a small correction to the SHG signal.^{30,54} The impact of this effect was also verified by comparing SHG measurements of monolayer MoS₂ on a glass and an Si/SiO₂ substrate (see Supporting Information). Figure 5a shows the wavelength dependence of d_s for 1T' MoTe₂ (blue circles) and monolayer MoS₂ (black squares). The MoS₂ measurements are in excellent agreement with refs 27 and 28, which provides support for our d_s 1T' MoTe₂ values. It is important to note that the d_s values

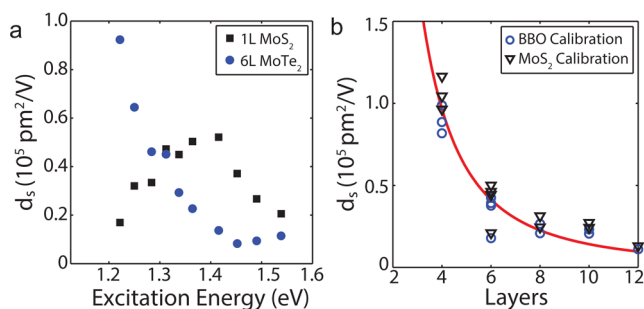


Figure 5. (a) Wavelength-dependent d_s of 1T' MoTe₂ (blue circles) and monolayer MoS₂ (black squares) calibrated using BBO. (b) Layer-dependent surface second-order susceptibility, d_s , of 1T' MoTe₂ calibrated using BBO (blue circles) and monolayer MoS₂ (black triangles). Solid line is empirically fit using $d_s(N) = 1.8 \times 10^6 N^{-2} \text{ pm}^2/\text{V}$.

reported in refs 29, 30, and 32 are an order of magnitude larger compared to refs 27 and 28 because different calibration procedures were used. Unlike the resonance for MoS₂, 1T' MoTe₂ shows d_s increases as the excitation wavelength increases as expected given the electronic states at $\approx 1 \text{ eV}$ at the Γ point.⁴⁸ The absolute tensor elements, d_{ij}^{abs} , of 1T' MoTe₂ are obtained using $d_{ij}^{\text{abs}} = d_s d_{ij}$ where d_{ij} is the normalized value discussed earlier. The layer dependence of d_s is shown in Figure 5b. The data were empirically fit using $d_s(N) = 1.8 \times 10^6 N^{-2} \text{ pm}^2/\text{V}$. Our measurements show that the peak d_s for 1T' MoTe₂ is of the same order of magnitude as MoS₂.

The crystal symmetry also determines the vibrational modes that are Raman active. Correctly assigning the Raman modes is particularly important for 1T' MoTe₂, because there is a large amount of discrepancy in the literature on symmetry and the number of modes.^{13,44–50} While density functional theory (DFT) has been used to attempt to assign the modes, the large number of active modes makes this task challenging, and the published results are inconsistent.^{44,45,50} As discussed above, the 1T' MoTe₂ with odd and even layers belong to the C_{2h}^2 and C_s^1 space groups, respectively. The Raman character tables are listed in the Supporting Information. Table 1 summarizes the

Table 1. Summary of Lattice Vibration Representations for N-Layer 1T' MoTe₂ with N Odd and N Even

	N odd (C_{2h}^2)	N even (C_s^1)
Raman	$6N A_g \oplus 3N B_g$	$6N A' \oplus 3N A''$
infrared	$(3N - 1) A_u \oplus (6N - 2) B_u$	$(6N - 2) A' \oplus (3N - 1) A''$
acoustic	$A_u \oplus 2 B_u$	$2 A' \oplus A''$

symmetry of the vibrational modes for C_{2h}^2 and C_s^1 space groups. From group theory analysis, we expect $6N$ Raman modes with A_g symmetry and $3N$ Raman modes with B_g symmetry for 1T' MoTe₂ with odd layers. For even layers, there should be $6N$ Raman modes with A' and $3N$ Raman modes with A'' symmetry. In both cases (even and odd layers), $9N$ Raman modes are expected. While the symmetry change for even and odd numbers of layers drastically affects the SHG signal, the point groups C_{2h} and C_s have the same Raman tensors, and no significant changes are expected in the Raman spectra. This means that, for any value of N , we should observe 9 Raman modes, each one with N -degeneracy. Experimentally, these Raman modes can be assigned by measuring the polarization dependence of the Raman signal.

Figure 6 a,b shows the polarization dependence of Raman scattering for the $N = 12$ region in Figure 1 d for parallel and crossed polarized configurations, respectively. The data were acquired in a backscattering geometry using a 532 nm laser that was focused onto the sample using a 0.75 NA objective with the laser power at 350 μW . For higher laser powers, we observed long exposure laser damage on thicker regions ($N > 10$). However, at this laser power, we still observed laser-induced damage for the $N = 3$ and 4 regions, but it does not impact the presented results (Supporting Information). The polarization measurements allowed for all the modes in 1T' MoTe₂ to be assigned, as indicated. These measurements resolve the discrepancy in the literature in identifying these modes and definitively assign the modes at ≈ 163 and $\approx 190 \text{ cm}^{-1}$ as A_g and B_g , respectively. Our assignments agree with the ones presented in ref 50.

Raman spectra, without a polarization analyzer, of several regions in Figure 1c with different number of layers are shown

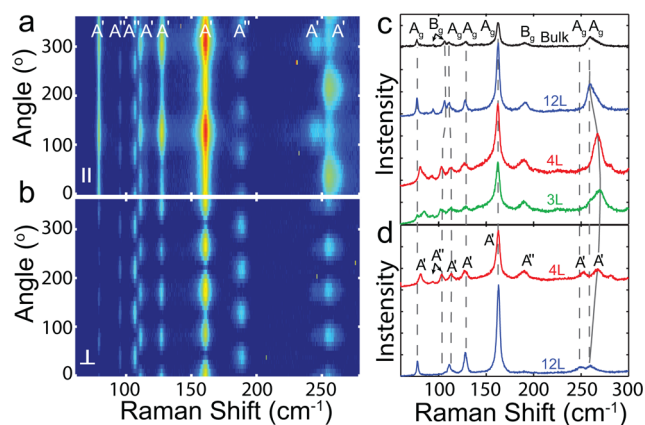


Figure 6. (a, b) Raman polarization dependence with the polarizer and analyzer parallel and crossed for the $N = 12$ region on a logarithmic scale. The Raman modes are labeled according to the symmetry. (c) Unpolarized Raman spectra of the bulk (black), $N = 12$ (blue), and $N = 4$ regions (red). (d) Example spectra of the $N = 4$ and 12 regions in a parallel configuration show the doublet at $\approx 260 \text{ cm}^{-1}$.

in Figure 6c. Despite the changes in the symmetry type, the Raman spectra are similar throughout as expected. However, we observe several spectral differences for thinner regions of the sample. The Raman modes are wider for the $N = 4$ region, which is likely due to tellurium evaporation.^{55,56} In addition, the higher energy mode in the doublet at $\approx 260 \text{ cm}^{-1}$ blue shifts, which was previously observed.⁴⁴ The spectral separation for the doublet at ≈ 107 and $\approx 111 \text{ cm}^{-1}$ increases, and the mode at $\approx 78 \text{ cm}^{-1}$ blue shifts. These shifts are likely due to differences in the interlayer interactions of the various modes. Figure 6d shows two example spectra for the $N = 4$ and 12 regions in a parallel configuration and shows that the peak at $\approx 260 \text{ cm}^{-1}$ is a doublet. Notably these two modes are both totally symmetric

(A' for even layers, and A_g for odd layers), but are out of phase, as shown in polarization maps (Figure 6 a,b). While other works have shown this doublet, the polarization dependence has not been previously characterized.^{13,14,50}

To gain a more detailed understanding of the Raman behavior of $1T'$ MoTe₂, the polarization dependence needs to be fit using the Raman tensors. Using the coordinate system defined in Figure 1, the Raman tensors are

$$\vec{\mathbf{R}}_{A_g} = \vec{\mathbf{R}}_{A'} = \begin{pmatrix} a & 0 & d \\ 0 & b & 0 \\ d & 0 & c \end{pmatrix} \quad (6)$$

$$\vec{\mathbf{R}}_{B_g} = \vec{\mathbf{R}}_{A''} = \begin{pmatrix} 0 & f & 0 \\ f & 0 & g \\ 0 & g & 0 \end{pmatrix} \quad (7)$$

Often the components of the Raman tensors are treated as real values, because the imaginary part of the Raman susceptibility is negligible for transparent materials. However, for materials with significant absorption, the components can be complex as was recently shown for black phosphorus and WTe₂.^{57,58} In this case, tensor elements are defined as $R_{ij} = |R_{ij}|e^{i\phi R_{ij}}$. Similar to the SHG analysis, the Raman signal is calculated using $S = |\hat{\epsilon}_s \cdot \vec{\mathbf{R}} \hat{\epsilon}_i|^2$, where the incident beam is $\hat{\epsilon}_i = [\cos \theta \sin \theta \ 0]$ and the scattered field is expressed as $\hat{\epsilon}_s = [\cos \theta \sin \theta \ 0]$ and $\hat{\epsilon}_s = [-\sin \theta \cos \theta \ 0]$ for parallel and cross-polarizations, respectively. Combining these expressions with eqs 6 and 7 leads to

$$S_{A_g}^{\parallel} = S_{A'}^{\parallel} = |a|^2 \cos^4 \theta + |b|^2 \sin^4 \theta + \frac{|a||b|}{2} \cos \phi_{ab} \sin^2 2\theta \quad (8)$$

$$S_{A_g}^{\perp} = S_{A'}^{\perp} = \frac{1}{4} (|a|^2 + |b|^2 - 2|a||b| \cos \phi_{ab}) \sin^2 2\theta \quad (9)$$

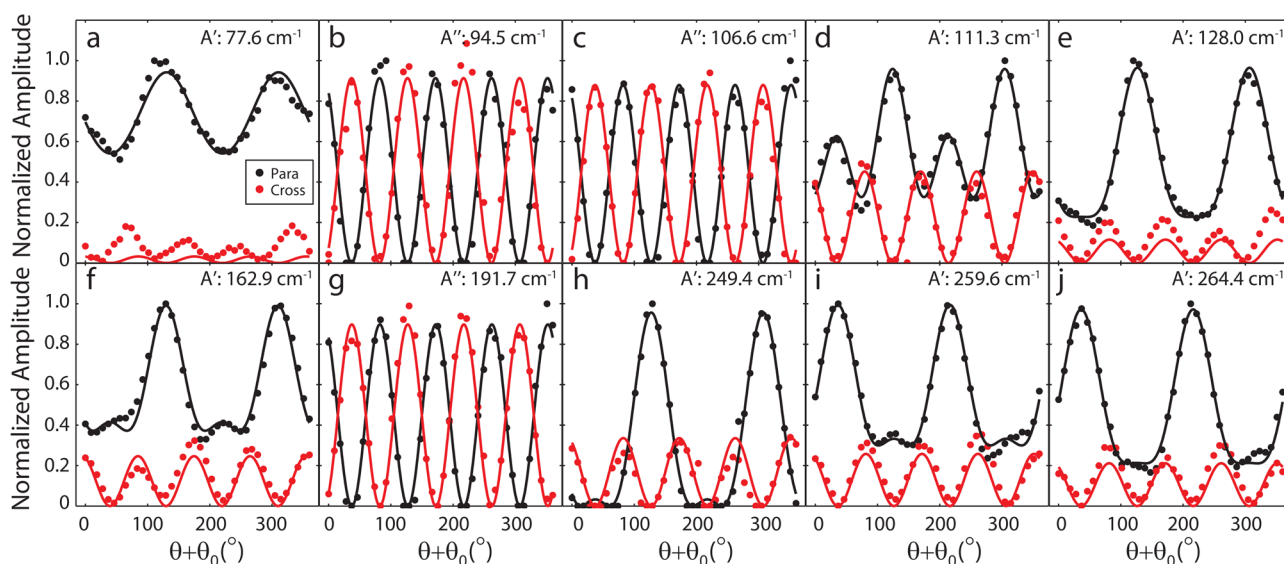


Figure 7. Normalized Raman amplitudes for parallel (red) and crossed (black) polarizations for the $N = 12$ region. The solid lines are the fits using the complex Raman tensors. The symmetry and frequency for each mode are labeled. The fits give $\theta_0 = -53^\circ$. Taking into account the difference in mounting angle between the SHG and Raman systems ($\approx -10^\circ$), the crystal orientations from the Raman measurements are in excellent agreement with the SHG measurements.

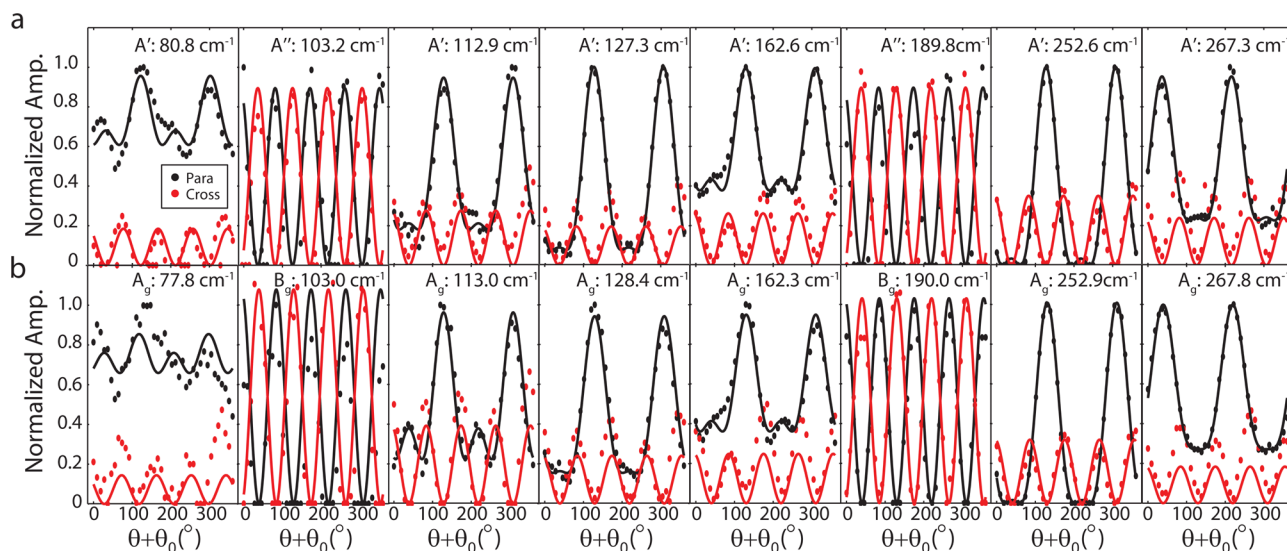


Figure 8. Normalized Raman amplitudes for parallel (red) and crossed (black) polarizations for the (a) $N = 4$ and (b) $N = 3$ regions of the sample in Figure 1. The solid lines are the fits using the complex Raman tensors. The symmetry and frequency for each mode are labeled. The fits give $\theta_0 = -52.5^\circ$. Taking into account the difference in mounting angle between the SHG and Raman systems ($\approx -10^\circ$), the crystal orientations from the Raman measurements are in excellent agreement with the SHG measurements.

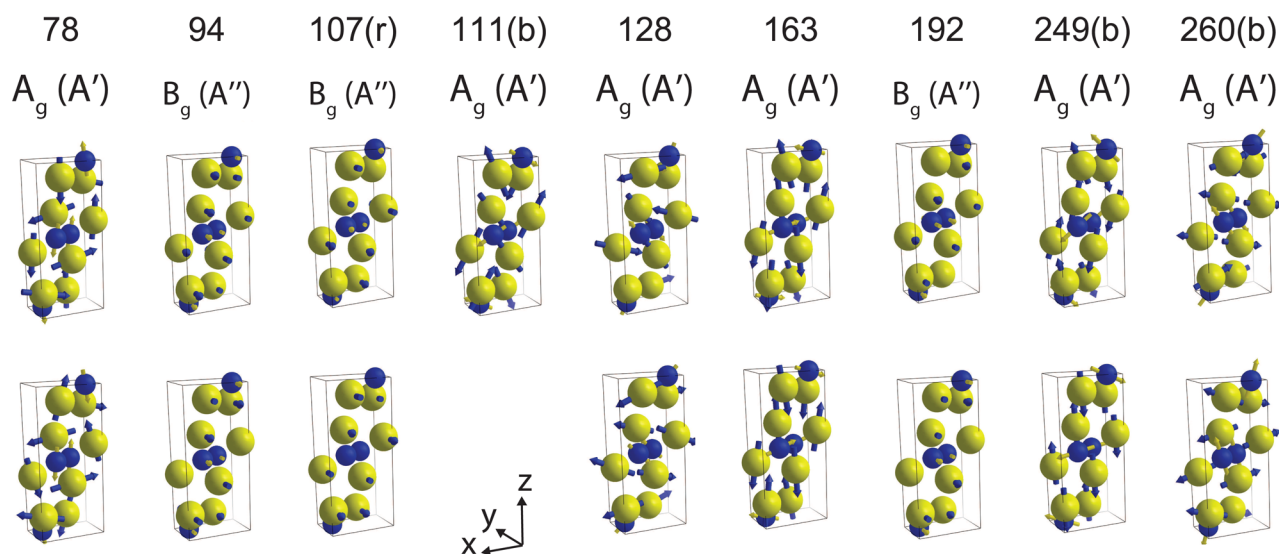


Figure 9. Summary of the Raman modes in N -layer $1T'$ MoTe₂ with N odd and N even. Modes that blue or red shift as the crystals get thinner are indicated with (b) and (r), respectively. Reported Raman shifts are for $N = 12$. Normal mode atomic displacements of bulk $1T'$ -MoTe₂ are shown as blue and yellow arrows for displacement of Te and Mo atoms, respectively. The magnitude of the displacements is proportional to the length of arrows. Blue and yellow spheres denote Mo and Te atoms, respectively. The primitive cells of bulk $1T'$ -MoTe₂ are shown by black boxes.

$$S_{B_g}^{\parallel} = S_{A''}^{\parallel} = |f|^2 \sin^2 2\theta \quad (10)$$

$$S_{B_g}^{\perp} = S_{A''}^{\perp} = |f|^2 \cos^2 2\theta \quad (11)$$

for the parallel and crossed polarized Raman signal for the two modes (see Methods section). ϕ_{ab} is the complex phase, and in the case of a real valued Raman tensor $\phi_{ab} = 0$. Notice that the complex phase cancels for the B_g and A'' modes.

The Raman spectra in Figures 6a,b were fit using Lorentzians, and the resulting amplitudes are plotted in Figure 7. The polarization dependence for the parallel (black) and crossed (red) polarized configurations was normalized by the maximum amplitude from the parallel configuration. Figure 7 plots 10 modes, where the first 9 are the modes pointed out in

Figure 6. The last peak was used to fit the high-energy shoulder on the peak at $\approx 260 \text{ cm}^{-1}$, which means for the $N = 12$ sample, the peaks from 250 to 260 cm^{-1} were treated as a triplet. This was not necessary for the $N = 4$ and 3 regions, which could indicate that there is an additional peak for thicker samples. The polarization dependence of the amplitudes was subsequently fit with eqs 8–11, shown as solid lines in Figure 7. While the real valued tensor overall fits the data, there are significant deviations, such as the secondary peaks and strong crossed polarized signal shown in Figure 7d and to a lesser extent in Figures 7f,i,j. This behavior shows that there is significant absorption in $1T'$ MoTe₂ and the complex nature of the Raman susceptibility is important. While this is an unusual behavior for transparent crystals, it is not altogether surprising

given the metallic nature of $1T'$ MoTe₂. The polarization measurements also show that all the A_g (A') modes are maximized for incident polarization along the zigzag direction (y axis), except the A_g (A') mode at ≈ 260 cm⁻¹. Similar plots for the $N = 4$ and 3 regions in Figure 1d are shown in Figures 8a,b, respectively. The peak shifts between the $N = 4$ and 3 regions agree with the trends shown in Figures 6c,d. The fits for the peak at ≈ 94 cm⁻¹ were omitted due to the low signal level. These polarization measurements directly demonstrate that the symmetry change from C_{2h}^2 ($N = 3$) to C_s^1 ($N = 4$) does not change the symmetry of the Raman modes. Additional Raman measurements from the sample in Figure 3 are in the Supporting Information. The Raman modes for the $N = 12$ region are summarized in Figure 9, and the red or blue shift with the number of layers is indicated.

In agreement with the experiments, DFT simulations of N -layer ($N = 1-4$ and ∞) $1T'$ MoTe₂ show that Raman spectra are similar despite the change in symmetry between odd and even number of layers, as shown in Figure 10. The DFT

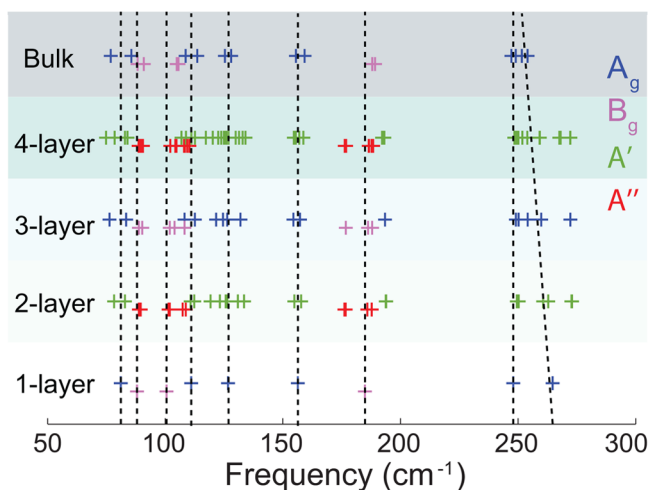


Figure 10. Raman active modes of N -layer MoTe₂ are plotted. Blue, magenta, green, and red symbols denote A_g, B_g, A', and A'' modes, respectively. The B_g and A' are offset from the A_g and A' modes for clarity. Dashed lines are drawn as guides for comparison of the peak frequencies between the five materials.

computed results also show that the N -layer $1T'$ MoTe₂ has a characteristic blue shift in the higher energy modes (around ≈ 260 cm⁻¹) and a spectral separation of the B_g and A_g modes at ≈ 105 and ≈ 110 cm⁻¹, respectively, as the number of layers decreases. Figure 10 shows that the blue shift in the higher energy modes is apparent when a comparison is made between 1-layer and bulk structure. In the 3-layer and 4-layer $1T'$ MoTe₂, the majority of the higher energy modes follow the same trend. A few outlying modes toward higher frequencies are predicted by our DFT calculations, which could either be the experimentally observed peak shoulders or modes with low Raman intensities. Note that the simulated normal-mode frequencies agree extremely well with the experimentally measured frequencies; for instance, the peak doublet at 259 cm⁻¹ is computed to be within 3% of the experimentally measured value, see Figure 9.

CONCLUSION

We have measured the polarization dependence of the SHG and Raman signal, from $1T'$ MoTe₂. These measurements

experimentally demonstrate the layer parity dependence of the inversion symmetry of $1T'$ MoTe₂ and resolve the discrepancy in the literature on the assignment of the Raman modes. The SHG analysis shows symmetry changing from odd (non-symmorphic monoclinic space group C_{2h}^2) to even (symmorphic monoclinic space group C_s^1) numbers of layers. The breakdown in the inversion symmetry for even numbers of layers allows for the crystal symmetry and orientation to be determined by means of polarization-dependent SHG measurements. Furthermore, the crystal orientation can also be independently determined using the anisotropic polarized Raman response. Despite the difference in the crystal symmetry for even and odd numbers of layers, all Raman modes can be explained by only two symmetry types. Finally, the $1T'$ phase is known to be a precursor to the T_d phase in MoTe₂, which shows promise as a Weyl semimetal, and thus SHG will also be an excellent tool for probing this transition.

METHODS

$1T'$ MoTe₂ Growth. MoTe₂ crystals were produced using CVT with iodine as the transport agent. MoTe₂ powder was synthesized by annealing molybdenum (99.999%) and tellurium (99.9%) powders mixed in a stoichiometric proportion at 750 °C for 72 h in an evacuated and sealed quartz ampule. Single crystals of MoTe₂ were created by sealing approximately 2 g of polycrystalline MoTe₂ powder and a small amount of iodine (99.8%, 4 mg/cm³) in evacuated 17 cm long quartz ampules. The ampules were placed in a furnace with a temperature gradient such that the MoTe₂ charge was kept at 1000 °C and temperature at the opposite end of the ampule was about 950 °C. Finally the ampule was quenched in ice water after 7 days of growth to retain the $1T'$ phase.

X-ray Diffraction. According to the $\theta-2\theta$ XRD scans, single crystals produced by the post-quenching method have crystallized in the $1T'$ structure (point group C_{2h}) with strong (0001) texture. The lattice parameters $a = 6.339(3)$ Å, $b = 3.466(4)$ Å, $c = 13.844(3)$ Å, and $\beta = 93.84(5)^\circ$ were obtained by the cell refinement method using MDI-JADE 6.5 software (Jade 6.5, Materials Data, Inc. Livermore, CA, 2015).⁵⁹

X-ray Photoelectron Spectroscopy. XPS was carried out using a monochromated Al K α source operated at 104 W and a hemispherical analyzer. Spectra were acquired at an analyzer pass energy of 10 eV, and the analysis area was approximately 0.1 mm \times 0.1 mm. Spectra were calibrated against C 1s (C-H, 284.8 eV) assigned to adventitious carbon.

MoTe₂ crystalline platelets were mounted on carbon tape and exfoliated immediately prior to loading into the vacuum chamber. The atomic composition of the surface was $29.3 \pm 5.1\%$ C, $22.0 \pm 1.9\%$ Mo, $3.2 \pm 1.8\%$ O, and $45.6 \pm 3.4\%$ Te. Errors reported are estimates of uncertainties associated with peak fitting and were calculated using a Monte Carlo analysis implemented in the CasaXPS software. One doublet in the Te region corresponding to $3d_{5/2}$ and $3d_{3/2}$ spin-orbit peaks was found at 572.5 and 582.9 eV ($\Delta = 10.4$ eV). Mo $3d_{5/2}$ and $3d_{3/2}$ components were found at 227.9 and 231.1 eV ($\Delta = 3.2$ eV). Peaks associated with TeO₂ were notably absent in the Te 3p and 3d spectra, but a small shoulder in the Mo 3d region ascribed to MoO_x was detectable. A small quantity of Te or Mo suboxide cannot be excluded based on the amount of oxygen measured on the surface.

Electron Backscatter Diffraction. Morphology of the samples was examined in a JEOL JSM-7100F field emission scanning electron microscope (FESEM). The identification of phases and crystallographic orientations of the flakes was performed by EBSD using an Oxford Instruments HKL Nordlys EBSD detector and NanoAnalysis AZtec 3.1 software.

Scanning Transmission Electron Microscopy. HAADF-STEM images were recorded on an aberration-corrected FEI Titan 80-300 operated at 300 kV, using a camera length of 100 mrad corresponding to inner and outer collection angles of 70.6 and 399.5 mrad, respectively. The sample has been crushed in ethanol, and a drop of

solution was placed on a 400-mesh TEM grid (Agar Inc.). Here, the observed HAADF-STEM intensity is proportional to the atomic number Z ($I \approx Z^\alpha$), where α is a proportionality factor between 1.5 and 2.⁶⁰ Given the differences between the atomic number of Mo ($Z_{\text{Mo}} = 42$) and Te ($Z_{\text{Te}} = 52$), the intensity variations can be attributed to the presence of two elements in the observed single crystals.

Atomic Force Microscope. The topographic images were acquired on an atomic force microscope operating in tapping mode. A mechanically stiff ($k = 42$ N/m) cantilever with a large driving amplitude and set point was used to mitigate the effects of the tip–material interactions and maintain a repulsive interaction.⁶¹ The thickness measurements were also compared to single layer graphene measurements, verified using Raman spectroscopy. To minimize oxidation, the samples were stored in a nitrogen environment between measurements.

Second Harmonic Generation and Raman Measurements. The Raman and SHG data were acquired by placing the sample on an x – y piezo scan stage. For the SHG measurements, the sample was excited by a femtosecond Ti:sapphire laser (≈ 75 fs, 80 MHz) centered at 992 nm using a microscope objective (0.75 NA). The average power was 0.6 mW at the sample. The sample was raster-scanned through the focus to build up images, and the resulting signal was collected using the same microscope objective and sent to either a single photon counting module with a narrow bandpass filter for rapid imaging or a spectrometer and a charge-coupled device (CCD). The Raman setup used 0.35 mW from a 532 nm laser using a microscope objective (0.75 NA). The spectra were acquired using a 500 mm focal length spectrometer with a 2400 lines/mm grating and CCD. Due to the low power levels, each spectral acquisition was 2 min. The spectra were calibrated using an Ar lamp, and the laser frequency was measured with a wavemeter. No signatures of MoO₂, MoO₃, or TeO₂ were measurable in the Raman spectra for the thicker samples. However, the small peak at ≈ 285 cm⁻¹ in the $N = 4$ sample could be from amorphous MoO₃ given the spectral location and lack of polarization dependence.

The SHG and Raman polarization dependence was measured by sending the linearly polarized excitation beam through a motorized achromatic halfwave plate, and the signal was analyzed using a motorized linear polarizer. Finally, the analyzed signal was sent through a multimode fiber that scrambled the polarization prior to the spectrometer to remove the polarization dependence of grating. We verified the system using a polarimeter and by measuring the polarization dependence of monolayer molybdenum disulfide (MoS₂) on the SHG and Raman instruments. Figure 2 was generated by taking a 10 s spectrum at each position; the resulting signal was fit with a Gaussian of fixed position and width. Despite low-power levels for the Raman measurements, some laser damage was observed for very thin samples (see Supporting Information).

Raman Mode Simulations. All simulations were based on DFT using the projector-augmented wave method as implemented in the plane-wave code VASP.^{62–65} All the simulations were performed using the vdW-DF-optB88 exchange–correlation functional.^{66–68} A k -point mesh of at least $10 \times 18 \times 5$ for the bulk 1T'-MoTe₂ and that of $10 \times 18 \times 1$ for the N -layer ($N = 1$ – 4) 1T'-MoTe₂ with a 600 eV energy cutoff resulted in an accuracy of the total energies of 1 meV/unitcell. The 5s²5p⁴ and 4d⁵5s electrons were considered as the valence electrons for Te and Mo, respectively. Including the semicore 4s²4p⁶ electrons for Mo had a negligible effect on the results, as, for instance, the lattice parameters of bulk 1T'-MoTe₂ changed by <0.1%. The n -layer MoTe₂ was simulated using a slab geometry with a vacuum spacing of 18 Å which ensures that the interactions between the periodic cells were negligible.

The bilayer, trilayer, and quad-layer of MoTe₂ were simulated in the same A-B stacking between the layers as in the bulk material. The structures were relaxed until the forces on the atoms were <1 meV/Å. The calculations of the phonon frequencies at the Gamma point were performed using DFT simulations (DFPT) on the primitive cells of the materials. All the measured peak positions of bulk 1T'-MoTe₂ were within 6% of the DFT computed values. Irreducible

representation of normal modes was obtained from the PHONOPY program⁶⁹ and the Bilbao Crystallographic Server.⁷⁰

ASSOCIATED CONTENT

Supporting Information

The Supporting Information is available free of charge on the ACS Publications website at DOI: 10.1021/acsnano.6b05127.

Raman character tables, DFT details, substrate effects on the SHG signal, laser damage data, flake orientation information, white light contrast, additional SHG measurements, and the topographic images for Figure 4 (PDF)

AUTHOR INFORMATION

Corresponding Author

*E-mail: stephan.stranick@nist.gov.

Notes

The authors declare no competing financial interest.

ACKNOWLEDGMENTS

R.B. acknowledges the NIST/National Research Council Research Associate Program (NRC RAP) for its support. P.M.V. acknowledges support from the GMU OSCAR Program. L.G.C. acknowledges the Brazilian agencies CNPq and FAPEMIG. A.B. acknowledges MGI. A.V.D., S.K., and I.K. acknowledge the support of Material Genome Initiative funding allocated to NIST. A.K.S. is funded by the Professional Research Experience Postdoctoral Fellowship under award no. 70NANB11H012. This research used computational resources provided by the Texas Advanced Computing Center under contract TG-DMR150006. This work used the Extreme Science and Engineering Discovery Environment (XSEDE), which was supported by National Science Foundation grant number ACI-1053575. We thank C. Janisch, I. Levin, J. Maslar, C. Michaels, and J. Ribeiro-Soares for fruitful discussions.

REFERENCES

- (1) Geim, A. K.; Grigorieva, I. V. Van der Waals Heterostructures. *Nature* **2013**, *499*, 419–425.
- (2) Mak, K. F.; Shan, J. Photonics and Optoelectronics of 2D Semiconductor Transition Metal Dichalcogenides. *Nat. Photonics* **2016**, *10*, 216–226.
- (3) Ali, M. N.; Xiong, J.; Flynn, S.; Tao, J.; Gibson, Q. D.; Schoop, L. M.; Liang, T.; Haldolaarachchige, N.; Hirschberger, M.; Ong, N. P.; Cava, R. J. Large, Non-Saturating Magnetoresistance in WTe₂. *Nature* **2014**, *514*, 205–208.
- (4) Kang, D.; Zhou, Y.; Yi, W.; Yang, C.; Guo, J.; Shi, Y.; Zhang, S.; Wang, Z.; Zhang, C.; Jiang, S.; Li, A.; Yang, K.; Wu, Q.; Zhang, G.; Sun, L.; Zhao, Z. Superconductivity Emerging from a Suppressed Large Magnetoresistant State in Tungsten Ditelluride. *Nat. Commun.* **2015**, *6*, 7804.
- (5) Qian, X.; Liu, J.; Fu, L.; Li, J. Quantum Spin Hall Effect in Two-Dimensional Transition Metal Dichalcogenides. *Science* **2014**, *346*, 1344–1347.
- (6) Sun, Y.; Wu, S.-C.; Ali, M. N.; Felser, C.; Yan, B. Prediction of Weyl Semimetal in Orthorhombic MoTe₂. *Phys. Rev. B: Condens. Matter Mater. Phys.* **2015**, *92*, 161107.
- (7) Soluyanov, A. A.; Gresch, D.; Wang, Z.; Wu, Q.; Troyer, M.; Dai, X.; Bernevig, B. A. Type-II Weyl Semimetals. *Nature* **2015**, *527*, 495–498.
- (8) Qi, Y.; Naumov, P. G.; Ali, M. N.; Rajamathi, C. R.; Schnelle, W.; Barkalov, O.; Hanfland, M.; Wu, S.-C.; Shekhar, C.; Sun, Y.; Süß, V.; Schmidt, M.; Schwarz, U.; Pippel, E.; Werner, P.; Hillebrand, R.;

Förster, T.; Kampert, E.; Parkin, S.; Cava, R. J.; et al. Superconductivity in Weyl Semimetal Candidate MoTe_2 . *Nat. Commun.* **2016**, *7*, 11038.

(9) Vellinga, M.; De Jonge, R.; Haas, C. Semiconductor to Metal Transition in MoTe_2 . *J. Solid State Chem.* **1970**, *2*, 299–302.

(10) Ruppert, C.; Aslan, O. B.; Heinz, T. F. Optical Properties and Band Gap of Single- and Few-Layer MoTe_2 Crystals. *Nano Lett.* **2014**, *14*, 6231–6236.

(11) Pradhan, N. R.; Rhodes, D.; Feng, S.; Xin, Y.; Memaran, S.; Moon, B.-H.; Terrones, H.; Terrones, M.; Balicas, L. Field-Effect Transistors Based on Few-Layered $\alpha\text{-MoTe}_2$. *ACS Nano* **2014**, *8*, 5911–5920.

(12) Dawson, W.; Bullett, D. Electronic Structure and Crystallography of MoTe_2 and WTe_2 . *J. Phys. C: Solid State Phys.* **1987**, *20*, 6159.

(13) Chen, S.-Y.; Goldstein, T.; Ramasubramanian, A.; Yan, J. Inversion-Symmetry-Breaking-Activated Shear Raman Bands in $T'\text{-MoTe}_2$. [arXiv:1602.03566](https://arxiv.org/abs/1602.03566), 2016.

(14) Joshi, J.; Stone, I.; Beams, R.; Krylyuk, S.; Kalish, I.; Davydov, A.; Vora, P. Phonon Anharmonicity in Bulk $T_d\text{-MoTe}_2$. *Appl. Phys. Lett.* **2016**, *109*, 031903.

(15) Chang, T.-R.; Xu, S.-Y.; Chang, G.; Lee, C.-C.; Huang, S.-M.; Wang, B.; Bian, G.; Zheng, H.; Sanchez, D. S.; Belopolski, I.; Alidoust, N.; Neupane, M.; Bansil, A.; Jeng, H.-T.; Lin, H.; Hasan, M. Z. Prediction of an Arc-Tunable Weyl Fermion Metallic State in $\text{Mo}_x\text{W}_{1-x}\text{Te}_2$. *Nat. Commun.* **2016**, *7*, 10639.

(16) Xu, N.; Wang, Z.; Weber, A.; Magrez, A.; Bugnon, P.; Berger, H.; Matt, C.; Ma, J.; Fu, B.; Lv, B. Q.; Plumb, N. C.; Radovic, M.; Pomjakushina, E.; Conder, K.; Qian, T.; Dil, J. H.; Mesot, J.; Ding, H.; Shi, M. Discovery of Weyl Semimetal State Violating Lorentz Invariance in MoTe_2 . [arXiv:1604.02116](https://arxiv.org/abs/1604.02116), 2016.

(17) Belopolski, I.; Xu, S.-Y.; Ishida, Y.; Pan, X.; Yu, P.; Sanchez, D. S.; Zheng, H.; Neupane, M.; Alidoust, N.; Chang, G.; et al. Fermi Arc Electronic Structure and Chern Numbers in the Type-II Weyl Semimetal Candidate $\text{Mo}_x\text{W}_{1-x}\text{Te}_2$. *Phys. Rev. B: Condens. Matter Mater. Phys.* **2016**, *94*, 085127.

(18) Wu, Y.; Jo, N. H.; Mou, D.; Huang, L.; Bud'ko, S.; Canfield, P.; Kaminski, A. Observation of Fermi Arcs in Type-II Weyl Semimetal Candidate WTe_2 . [arXiv:1604.05176](https://arxiv.org/abs/1604.05176), 2016.

(19) Wang, C.; Zhang, Y.; Huang, J.; Nie, S.; Liu, G.; Liang, A.; Zhang, Y.; Shen, B.; Liu, J.; Hu, C.; Ding, Y.; Liu, D.; Hu, Y.; He, S.; Zhao, L.; Yu, L.; Hu, J.; Wei, J.; Mao, Z.; Shi, Y. et al. Spectroscopic Evidence of Type II Weyl Semimetal State in WTe_2 . [arXiv:1604.04218](https://arxiv.org/abs/1604.04218), 2016.

(20) Deng, K.; Wan, G.; Deng, P.; Zhang, K.; Ding, S.; Wang, E.; Yan, M.; Huang, H.; Zhang, H.; Xu, Z.; Denlinger, J.; Fedorov, A.; Yang, H.; Duan, W.; Yao, H.; Wu, Y.; Fan, Y. S.; Zhang, H.; Chen, X.; Zhou, S. Experimental Observation of Topological Fermi Arcs in Type-II Weyl Semimetal MoTe_2 . [arXiv:1603.08508](https://arxiv.org/abs/1603.08508), 2016.

(21) Liang, A.; Huang, J.; Nie, S.; Ding, Y.; Gao, Q.; Hu, C.; He, S.; Zhang, Y.; Wang, C.; Shen, B.; Liu, J.; Ai, P.; Yu, L.; Sun, X.; Zhao, W.; Lv, S.; Liu, D.; Li, C.; Zhang, Y. Y.; Hu, Y. et al. Electronic Evidence for Type II Weyl Semimetal State in MoTe_2 . [arXiv:1604.01706](https://arxiv.org/abs/1604.01706), 2016.

(22) Jiang, J.; Liu, Z.; Sun, Y.; Yang, H.; Rajamathi, R.; Qi, Y.; Yang, L.; Chen, C.; Peng, H.; Hwang, C. C.; Sun, S. Z.; Mo, S. K.; Vobornik, I.; Fujii, J.; Parkin, S. S. P.; Felser, C.; Yan, B. H.; Chen, Y. L. Observation of the Type-II Weyl Semimetal Phase in MoTe_2 . [arXiv:1604.00139](https://arxiv.org/abs/1604.00139), 2016.

(23) Huang, L.; McCormick, T. M.; Ochi, M.; Zhao, Z.; Suzuki, M.-t.; Arita, R.; Wu, Y.; Mou, D.; Cao, H.; Yan, J.; Trivedi, N.; Kaminski, A. Spectroscopic Evidence for Type II Weyl Semimetal State in MoTe_2 . [arXiv:1603.06482](https://arxiv.org/abs/1603.06482), 2016.

(24) Tamai, A.; Wu, Q.; Cucchi, I.; Bruno, F.; Ricco, S.; Kim, T.; Hoesch, M.; Barreteau, C.; Giannini, E.; Bernard, C.; Soluyanov, A. A.; Baumberg, F. Fermi Arcs and Their Topological Character in the Candidate Type-II Weyl Semimetal MoTe_2 . [arXiv:1604.08228](https://arxiv.org/abs/1604.08228), 2016.

(25) Tongay, S.; Sahin, H.; Ko, C.; Luce, A.; Fan, W.; Liu, K.; Zhou, J.; Huang, Y.-S.; Ho, C.-H.; Yan, J. Monolayer Behaviour in Bulk ReS_2 Due to Electronic and Vibrational Decoupling. *Nat. Commun.* **2014**, *5*, 3252.

(26) Lorchat, E.; Froehlicher, G.; Berciaud, S. Splitting of Interlayer Shear Modes and Photon Energy Dependent Anisotropic Raman Response in N-Layer ReSe_2 and ReS_2 . *ACS Nano* **2016**, *10*, 2752–2760.

(27) Li, Y.; Rao, Y.; Mak, K. F.; You, Y.; Wang, S.; Dean, C. R.; Heinz, T. F. Probing Symmetry Properties of Few-Layer MoS_2 and h-BN by Optical Second-Harmonic Generation. *Nano Lett.* **2013**, *13*, 3329–3333.

(28) Malard, L. M.; Alencar, T. V.; Barboza, A. P. M.; Mak, K. F.; de Paula, A. M. Observation of Intense Second Harmonic Generation from MoS_2 Atomic Crystals. *Phys. Rev. B: Condens. Matter Mater. Phys.* **2013**, *87*, 201401.

(29) Kumar, N.; Najmaei, S.; Cui, Q.; Ceballos, F.; Ajayan, P. M.; Lou, J.; Zhao, H. Second Harmonic Microscopy of Monolayer MoS_2 . *Phys. Rev. B: Condens. Matter Mater. Phys.* **2013**, *87*, 161403.

(30) Janisch, C.; Wang, Y.; Ma, D.; Mehta, N.; Elías, A. L.; Perea-López, N.; Terrones, M.; Crespi, V.; Liu, Z. Extraordinary Second Harmonic Generation in Tungsten Disulfide Monolayers. *Sci. Rep.* **2014**, *4*, 5530.

(31) Wang, G.; Marie, X.; Gerber, I.; Amand, T.; Lagarde, D.; Bouet, L.; Vidal, M.; Balocchi, A.; Urbaszek, B. Giant Enhancement of the Optical Second-Harmonic Emission of WSe_2 Monolayers by Laser Excitation at Exciton Resonances. *Phys. Rev. Lett.* **2015**, *114*, 097403.

(32) Ribeiro-Soares, J.; Janisch, C.; Liu, Z.; Elías, A.; Dresselhaus, M.; Terrones, M.; Caçado, L.; Jorio, A. Second Harmonic Generation in WSe_2 . *2D Mater.* **2015**, *2*, 045015.

(33) David, S. N.; Zhai, Y.; van der Zande, A. M.; O'Brien, K.; Huang, P. Y.; Chenet, D. A.; Hone, J. C.; Zhang, X.; Yin, X. Rapid, All-Optical Crystal Orientation Imaging of Two-Dimensional Transition Metal Dichalcogenide monolayers. *Appl. Phys. Lett.* **2015**, *107*, 111902.

(34) Ferrari, A. C.; Basko, D. M. Raman Spectroscopy as a Versatile Tool for Studying the Properties of Graphene. *Nat. Nanotechnol.* **2013**, *8*, 235–246.

(35) Beams, R.; Caçado, L. G.; Novotny, L. Raman Characterization of Defects and Dopants in Graphene. *J. Phys.: Condens. Matter* **2015**, *27*, 083002.

(36) Zhang, X.; Qiao, X.-F.; Shi, W.; Wu, J.-B.; Jiang, D.-S.; Tan, P.-H. Phonon and Raman Scattering of Two-Dimensional Transition Metal Dichalcogenides from Monolayer, Multilayer to Bulk Material. *Chem. Soc. Rev.* **2015**, *44*, 2757–2785.

(37) Luo, X.; Zhao, Y.; Zhang, J.; Toh, M.; Kloc, C.; Xiong, Q.; Quek, S. Y. Effects of Lower Symmetry and Dimensionality on Raman Spectra in Two-Dimensional WSe_2 . *Phys. Rev. B: Condens. Matter Mater. Phys.* **2013**, *88*, 195313.

(38) Ribeiro-Soares, J.; Almeida, R.; Barros, E.; Araujo, P.; Dresselhaus, M.; Caçado, L.; Jorio, A. Group Theory Analysis of Phonons in Two-Dimensional Transition Metal Dichalcogenides. *Phys. Rev. B: Condens. Matter Mater. Phys.* **2014**, *90*, 115438.

(39) Ribeiro-Soares, J.; Almeida, R.; Cancado, L.; Dresselhaus, M.; Jorio, A. Group Theory for Structural Analysis and Lattice Vibrations in Phosphorene Systems. *Phys. Rev. B: Condens. Matter Mater. Phys.* **2015**, *91*, 205421.

(40) Kolobov, A. V.; Tominaga, J. *Two-Dimensional Transition-Metal Dichalcogenides*; Springer International Publishing: Switzerland, 2016; pp 227–294.

(41) Saito, R.; Tatsumi, Y.; Huang, S.; Ling, X.; Dresselhaus, M. Raman Spectroscopy of Transition Metal Dichalcogenides. *J. Phys.: Condens. Matter* **2016**, *28*, 353002.

(42) Yamamoto, M.; Wang, S. T.; Ni, M.; Lin, Y.-F.; Li, S.-L.; Aikawa, S.; Jian, W.-B.; Ueno, K.; Wakabayashi, K.; Tsukagoshi, K. Strong Enhancement of Raman Scattering from a Bulk-Inactive Vibrational Mode in Few-Layer MoTe_2 . *ACS Nano* **2014**, *8*, 3895–3903.

(43) Guo, H.; Yang, T.; Yamamoto, M.; Zhou, L.; Ishikawa, R.; Ueno, K.; Tsukagoshi, K.; Zhang, Z.; Dresselhaus, M. S.; Saito, R. Double Resonance Raman Modes in Monolayer and Few-Layer MoTe_2 . *Phys. Rev. B: Condens. Matter Mater. Phys.* **2015**, *91*, 205415.

(44) Keum, D. H.; Cho, S.; Kim, J. H.; Choe, D.-H.; Sung, H.-J.; Kan, M.; Kang, H.; Hwang, J.-Y.; Kim, S. W.; Yang, H.; Chang, K. J.; Lee, Y.

H. Bandgap Opening in Few-Layered Monoclinic MoTe₂. *Nat. Phys.* **2015**, *11*, 482–486.

(45) Cho, S.; Kim, S.; Kim, J. H.; Zhao, J.; Seok, J.; Keum, D. H.; Baik, J.; Choe, D.-H.; Chang, K.; Suenaga, K.; Kim, S. W.; Lee, Y. H.; Yang, H. Phase Patterning for Ohmic Homo Junction Contact in MoTe₂. *Science* **2015**, *349*, 625–628.

(46) Park, J. C.; Yun, S. J.; Kim, H.; Park, J.-H.; Chae, S. H.; An, S.-J.; Kim, J.-G.; Kim, S. M.; Kim, K. K.; Lee, Y. H. Phase-Engineered Synthesis of Centimeter-Scale 1T'- and 2H-Molybdenum Ditelluride Thin Films. *ACS Nano* **2015**, *9*, 6548–6554.

(47) Zhou, L.; Xu, K.; Zubair, A.; Liao, A. D.; Fang, W.; Ouyang, F.; Lee, Y.-H.; Ueno, K.; Saito, R.; Palacios, T.; Kong, J.; Dresselhaus, M. S. Large-Area Synthesis of High-Quality Uniform Few-Layer MoTe₂. *J. Am. Chem. Soc.* **2015**, *137*, 11892–11895.

(48) Kan, M.; Nam, H. G.; Lee, Y. H.; Sun, Q. Phase Stability and Raman Vibration of the Molybdenum Ditelluride (MoTe₂) Monolayer. *Phys. Chem. Chem. Phys.* **2015**, *17*, 14866–14871.

(49) Sun, Y.; Wang, Y.; Sun, D.; Carvalho, B. R.; Read, C. G.; Lee, C.-h.; Lin, Z.; Fujisawa, K.; Robinson, J. A.; Crespi, V. H.; Terrones, M.; Schaak, R. E. Low-Temperature Solution Synthesis of Few-Layer 1T'-MoTe₂ Nanostructures Exhibiting Lattice Compression. *Angew. Chem., Int. Ed.* **2016**, *55*, 2830–2834.

(50) Naylor, C. H.; Parkin, W. M.; Ping, J.; Gao, Z.; Zhou, Y. R.; Kim, Y.; Streller, F.; Carpick, R. W.; Rappe, A. M.; Drndic, M.; Kikkawa, J. M.; Johnson, A. T. C. Monolayer Single-Crystal 1T'-MoTe₂ Grown by Chemical Vapor Deposition Exhibits a Weak Antilocalization Effect. *Nano Lett.* **2016**, *16*, 4297.

(51) *International Tables for Crystallography*, 5th ed.; Hahn, T., Ed.; Springer: Dordrecht, The Netherlands, 2005; Vol. A: Space-Group Symmetry.

(52) Brown, B. E. The Crystal Structures of WTe₂ and High-Temperature MoTe₂. *Acta Crystallogr.* **1966**, *20*, 268–274.

(53) Boyd, R. W. *Nonlinear Optics*, 3rd ed.; Academic Press: San Diego, CA, 2008.

(54) Kudryavtsev, A.; Lavrov, S.; Shestakova, A.; Kulyuk, L.; Mishina, E. Second Harmonic Generation in Nanoscale Films of Transition Metal Dichalcogenide: Accounting for Multipath Interference. *AIP Adv.* **2016**, *6*, 095306.

(55) Clarke, R.; Marseglia, E.; Hughes, H. A Low-Temperature Structural Phase Transition in β -MoTe₂. *Philos. Mag. B* **1978**, *38*, 121–126.

(56) Song, S.; Keum, D. H.; Cho, S.; Perello, D.; Kim, Y.; Lee, Y. H. Room Temperature Semiconductor-Metal Transition of MoTe₂ Thin Films Engineered by Strain. *Nano Lett.* **2016**, *16*, 188–193.

(57) Ribeiro, H. B.; Pimenta, M. A.; de Matos, C. J.; Moreira, R. L.; Rodin, A. S.; Zapata, J. D.; de Souza, E. A.; Castro Neto, A. H. Unusual Angular Dependence of the Raman Response in Black Phosphorus. *ACS Nano* **2015**, *9*, 4270–4276.

(58) Song, Q.; Pan, X.; Wang, H.; Zhang, K.; Tan, Q.; Li, P.; Wan, Y.; Wang, Y.; Xu, X.; Lin, M.; Wan, X.; Song, F.; Dai, L. The In-Plane Anisotropy of WTe₂ Investigated by Angle-Dependent and Polarized Raman Spectroscopy. *Sci. Rep.* **2016**, *6*, 29254.

(59) Disclaimer: Certain commercial equipment, instruments, or materials are identified in this paper in order to specify the experimental procedure adequately. Such identification is not intended to imply recommendation or endorsement by the National Institute of Standards and Technology nor is it intended to imply that the materials or equipment identified are necessarily the best available for the purpose.

(60) Erni, R. *Aberration Corrected Imaging in Transmission Electron Microscopy*; Imperial College Press: London, 2010.

(61) Nemes-Incze, P.; Osváth, Z.; Kamarás, K.; Biró, L. Anomalies in Thickness Measurements of Graphene and Few Layer Graphite Crystals by Tapping Mode Atomic Force Microscopy. *Carbon* **2008**, *46*, 1435–1442.

(62) Kresse, G.; Hafner, J. Ab Initio Molecular Dynamics for Liquid Metals. *Phys. Rev. B: Condens. Matter Mater. Phys.* **1993**, *47*, 558.

(63) Kresse, G.; Hafner, J. Ab Initio Molecular-Dynamics Simulation of the Liquid-Metal-Amorphous-Semiconductor Transition in Germanium. *Phys. Rev. B: Condens. Matter Mater. Phys.* **1994**, *49*, 14251.

(64) Kresse, G.; Furthmüller, J. Efficiency of Ab-Initio Total Energy Calculations for Metals and Semiconductors Using a Plane-Wave Basis Set. *Comput. Mater. Sci.* **1996**, *6*, 15–50.

(65) Kresse, G.; Furthmüller, J. Efficient Iterative Schemes for Ab Initio Total-Energy Calculations Using a Plane-Wave Basis Set. *Phys. Rev. B: Condens. Matter Mater. Phys.* **1996**, *54*, 11169.

(66) Dion, M.; Rydberg, H.; Schröder, E.; Langreth, D. C.; Lundqvist, B. I. Van der Waals Density Functional for General Geometries. *Phys. Rev. Lett.* **2004**, *92*, 246401.

(67) Román-Pérez, G.; Soler, J. M. Efficient Implementation of a Van der Waals Density Functional: Application to Double-Wall Carbon Nanotubes. *Phys. Rev. Lett.* **2009**, *103*, 096102.

(68) Klimeš, J. c. v.; Bowler, D. R.; Michaelides, A. Van der Waals Density Functionals Applied to Solids. *Phys. Rev. B: Condens. Matter Mater. Phys.* **2011**, *83*, 195131.

(69) Togo, A.; Tanaka, I. First Principles Phonon Calculations in Materials Science. *Scr. Mater.* **2015**, *108*, 1–5.

(70) Aroyo, M. I.; Kirov, A.; Capillas, C.; Perez-Mato, J.; Wondratschek, H. Bilbao Crystallographic Server. II. Representations of Crystallographic Point Groups and Space Groups. *Acta Crystallogr., Sect. A: Found. Crystallogr.* **2006**, *62*, 115–128.

(71) Chen, S. Y.; Goldstein, T.; Venkataraman, D.; Ramasubramanian, A.; Yan, J. Activation of New Raman Modes by Inversion Symmetry Breaking in Type II Weyl Semimetal Candidate T'-MoTe₂. *Nano Lett.* **2016**, *16*, 5852–5860.

NOTE ADDED IN PROOF

During the review process ref 71 showed similar polarized Raman results for bulk 1T' MoTe₂.

Supporting information for:
Characterization of Few-Layer 1T' MoTe₂ by
Polarization-Resolved Second Harmonic
Generation and Raman Scattering

Ryan Beams,[†] Luiz Gustavo Cançado,[‡] Sergiy Krylyuk,^{†,¶} Irina Kalish,[†] Berç Kalanyan,[†] Arunima K. Singh,[†] Kamal Choudhary,[†] Alina Bruma,[†] Patrick M. Vora,[§] Francesca Tavazza,[†] Albert V. Davydov,[†] and Stephan J. Stranick*,[†]

[†]*Material Measurement Laboratory, National Institute of Standards and Technology,
Gaithersburg, MD 20899, U.S.A.*

[‡]*Departamento de Física, Universidade Federal de Minas Gerais, Belo Horizonte, MG
30123-970, Brazil*

[¶]*Theiss Research, La Jolla, CA, 92037 USA*

[§]*Department of Physics and Astronomy, George Mason University, VA, USA*

E-mail: stephan.stranick@nist.gov

Character tables

Table S1: Character table for the C_{2h} point group, corresponding to the N -layer $1T'$ MoTe₂ with N odd (C_{2h}^2 , or $P2_1/m$ space group symmetry). E is the identity, C_{2y} is a two-fold rotation axis along y , σ_{xz} is an horizontal plane mirror (parallel to xz), and i is the inversion. These symmetry elements, as well as the Cartesian coordinates are defined in Figs. 1 a,b. The first column indicates the irreducible representations, and the last column gives the corresponding basis functions.^{S1}

	E	C_{2y}	σ_{xz}	i	
A_g	1	1	1	1	x^2, y^2, z^2, xz
B_g	1	1	-1	-1	y
A_u	1	-1	-1	1	xy, yz
B_u	1	-1	1	-1	x, z

Table S2: Character table for the C_s point group, corresponding to the N -layer $1T'$ MoTe₂ with N even (C_s^1 , or Pm space group symmetry). Same geometrical definitions as for Table S1 apply.^{S1}

	E	σ_{xz}	
A'	1	1	x, z, x^2, y^2, z^2, xz
A''	1	-1	y, xy, yz

Tables S1 and S2 using the coordinate system defined in Figure 1 of the main text, which is rotated compared to many reference books. Similarly, the Raman tensors in Eqs.6 and 7 are rotated to keep the coordinate system consistent throughout the work.

Density-functional theory simulations of Raman modes

Table S3 shows the lattice constants, a , b and β , and symmetry of $1T'$ -MoTe₂ as a function of number of layers. The lattice parameters change minimally as the number of layers increases with the most noticeable change in the b -lattice parameter, the b -lattice parameter of 1-layer $1T'$ -MoTe₂ being 1.36% smaller than that of the bulk $1T'$ -MoTe₂. The lattice parameters computed from the DFT simulations have an excellent agreement with the experimentally

measured values, differing by $< 2\%$. The 1-layer, 3-layer and bulk structures are found to have a C_{2h}^2 space group and the 2-layer and 4-layer structures have the C_s^1 space group.

Table S3: Lattice vectors, a , b and c in Å, angle β in $^\circ$ and the symmetry of of N -layer $1T'$ -MoTe₂ as computed from DFT simulations.

	a	b	β	Symmetry
Bulk	6.361	3.526	92.18	C_{2h}^1 (P2 ₁ /m, #11)
	$c = 14.137$			
1-layer	6.356	3.478	92.15	C_{2h}^1 (P2 ₁ /m, #11)
2-layer	6.352	3.496	92.15	C_s^1 (Pm, #6)
3-layer	6.353	3.504	92.15	C_{2h}^1 (P2 ₁ /m, #11)
4-layer	6.354	3.511	92.15	C_s^1 (Pm, #6)

Substrate effects and experimental validation using MoS₂

The second order susceptibility, $\chi^{(2)}$, of $1T'$ MoTe₂ was calibrated by measuring monolayer MoS₂ under the same measurement conditions. Since the MoTe₂ samples were prepared on an SiO₂/Si substrate, there was an additional contribution to the SHG signal due to the cavity created by the SiO₂/Si. While this term has been shown to be negligible,^{S2-S4} we prepared monolayer MoS₂ samples on glass and SiO₂/Si to experimentally measure the cavity contribution. In Figure S1 the top and bottom rows show the samples on glass and SiO₂/Si, respectively. Figure S1 a,b show the white light images of the MoS₂ samples with the monolayer regions labeled. The single layer regions were verified using photoluminescence (PL) and Raman spectroscopy. The PL of the monolayer regions with the A and B excitons labeled are shown in Figure S1 b,c. Figure S1 d,e shows the Raman spectra. The PL^{S5} and Raman^{S5,S6} confirmed that the regions of interest are monolayer. Finally, SHG images on the same intensity scale of both regions are shown in Figure S1 f,g with linecuts shown in the insets. In this case no analyzer was used to remove the polarization dependence. These images show that the SHG signals are equivalent within our measurement accuracy. Therefore the signal enhancement from the cavity is negligible, as expected. Finally the SHG polar maps of the monolayer flake with the polarizer and analyzer parallel (black) and

crossed (red) are shown in Figure S1.

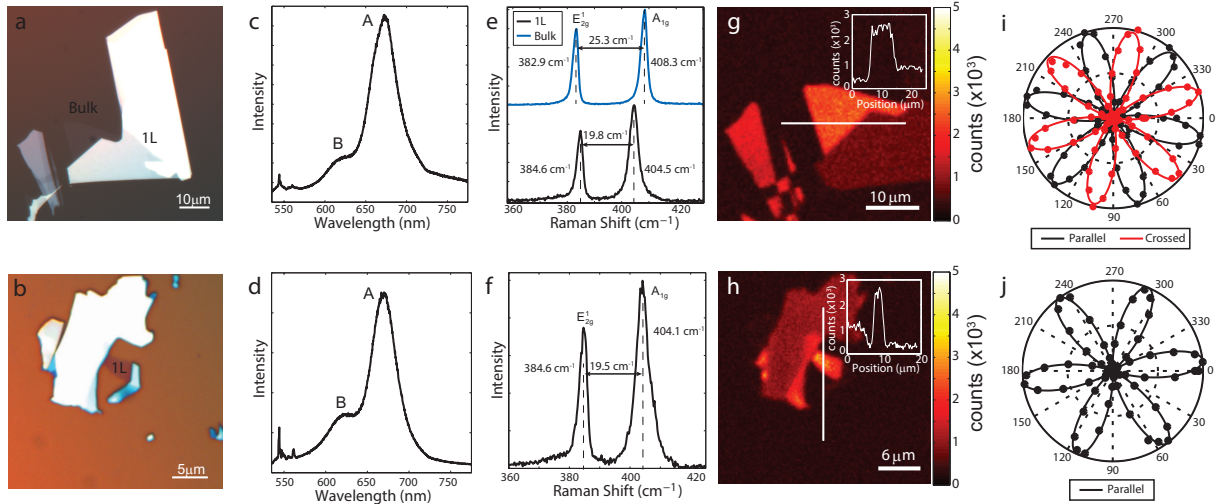


Figure S1: Characterization of monolayer MoS_2 samples. The top (bottom) row is a sample exfoliated on glass (SiO_2/Si). (a),(b) White light images of the MoS_2 samples with the monolayer sections labeled. (b),(c) Photoluminescence spectra of the two monolayer samples. (d),(e) Raman spectra of the two monolayer samples. (g),(h) SHG images of the two samples on the same intensity scale. (i) SHG polar maps of the monolayer flake with the polarizer and analyzer parallel (black) and crossed (red).

Laser damage and Raman measurement of additional flake

Figure S2 shows the Raman polarization dependence of the $N = 4$ sample from Figure 3 in the main text. The top set of plots is the raw data and a significant signal decrease is observed due to laser damage. The open circle data points were used for the damage plots in Figure S4. These points show the exponential decrease in the signal level. In order to plot the modes with A_g on the same scale as the modes with B_g symmetry, the first maximum for the A_g modes was scaled by the fractional signal decrease of the B_g by that time in the acquisition. The lower set of plots was corrected by dividing each data point by the fit from the exponential decay. After this correction, the Raman polarization equations from the main text were used to fit this data. There are a few differences from the polarization dependence for the $N = 12$ region in the main text. First, only one Lorentzian was used

to fit the peak at $\approx 260 \text{ cm}^{-1}$ since a high energy tail was not observed. Also, an additional Lorentzian centered at 156 cm^{-1} was used to fit the laser damage induced broad shoulder that developed on the $\approx 160 \text{ cm}^{-1}$ peak. The amplitude of that peak increases during the polarization measurements as expected for laser damage. From the Raman measurements, $\theta_0 = -54^\circ$, which is in excellent agreement with the SHG images once the sample mounting angle is taken into account (see below).

The final aspect of the Raman measurements that we will discuss is the low damage threshold for this material. For the 2H phase, oxidation^{S7} and laser induced phase changes have been reported;^{S8} however, damage and oxidation have not been reported for 1T'. Our sample was stored in an N₂ environment except for during measurements to try to minimize oxidation. As mentioned in the main text, the samples were measured using $350 \mu\text{W}$ with a 0.75NA objective, which is between a factor 5 to 10 lower power than is commonly used for other TMDs and graphene. This power was chosen because higher powers showed laser damage over several hour exposures for bulk crystals, which manifested as a decrease in the Raman signal. At $350 \mu\text{W}$ no appreciable laser damage was observed for the $N = 12$ region, as can be seen by the constant amplitudes in Figure 4 of the main text. However, for the $N = 4$ and $N = 3$ regions an exponential decrease in the Raman signal was observed, as shown in the raw data in Figure S3.

Figure S4a,b shows the initial Raman spectra of the $N = 4$ region and after 80 min of laser exposure, both of them on the same intensity scale. The Raman signal decreased for all the modes and a high and low energy shoulder developed on the mode at $\approx 80 \text{ cm}^{-1}$ and $\approx 160 \text{ cm}^{-1}$, respectively. To better illustrate the shoulders, a difference spectra of Figure S4a and b after re-scaling is shown in blue. The absence of Raman peaks from $300\text{--}500 \text{ cm}^{-1}$ suggests that the shoulders are not caused by TeO₂^{S9} or MoO₂.^{S10,S11} MoO₃ has peaks at $\approx 89 \text{ cm}^{-1}$ and $\approx 160 \text{ cm}^{-1}$ in agreement with the spectral location of the shoulders. However, MoO₃ also has a peak at $\approx 285 \text{ cm}^{-1}$ and the amplitude of the slight peak at that

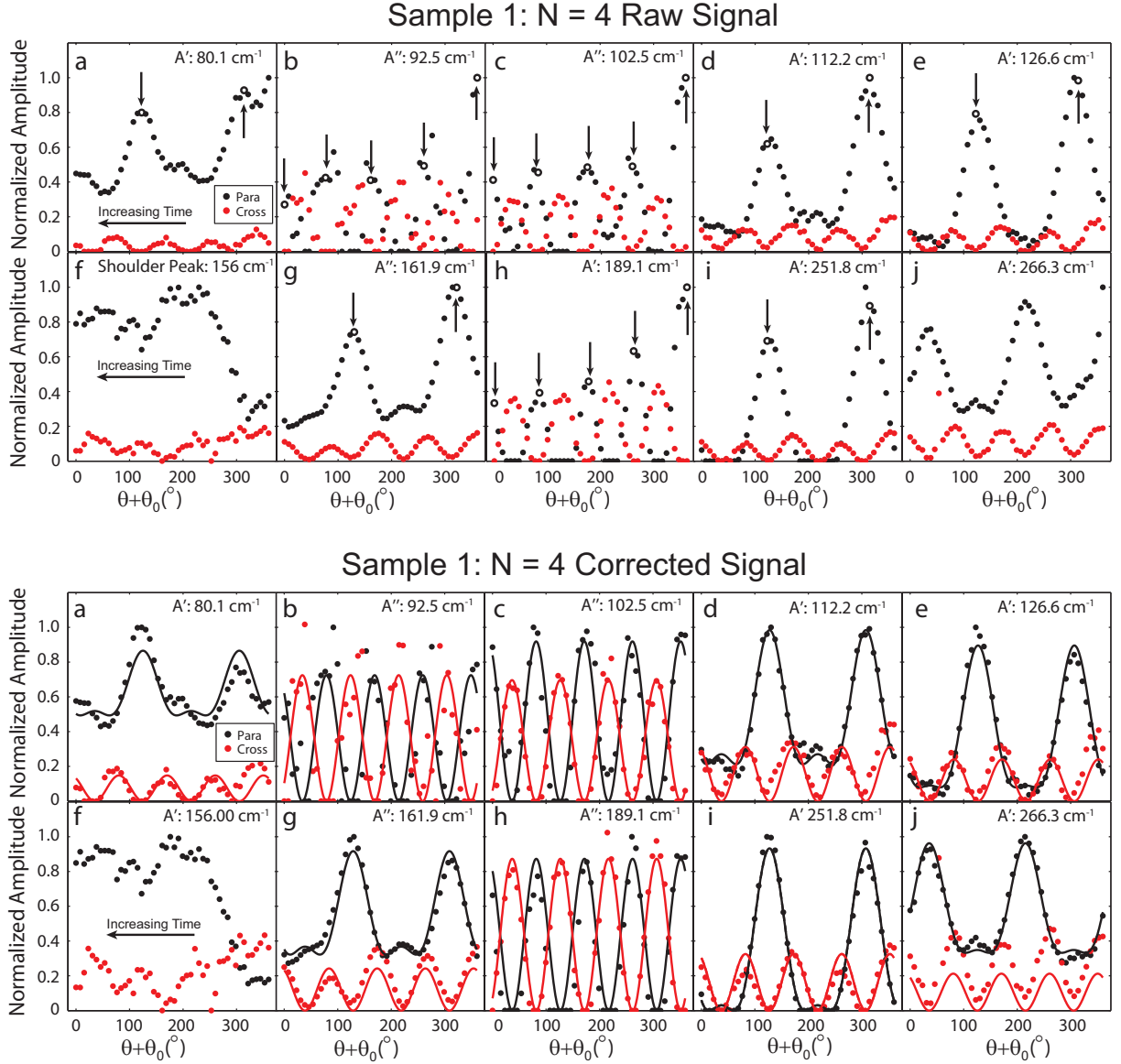


Figure S2: Normalized Raman amplitudes for parallel (red) and crossed (black) polarizations for the $N = 4$ region for Sample 1. The symmetry and position for each mode are labeled. The top set is the raw data and the bottom set is after correcting for the signal decrease. The fits using the complex Raman tensors (solid lines) are shown.

spectral location does not increase. Amorphous tellurium also has peaks at approximately the same spectral locations,^{S12} which is in agreement with a tellurium evaporation mechanism. Tellurium evaporation and oxidation are both candidates for the decrease in the MoTe₂ Raman signal. The time dependent decrease in the Raman signal is plotted in Figure S4 c,d for the $N = 4$ region in Figure 1 d as well as an additional $N = 4$ region. Each mode is

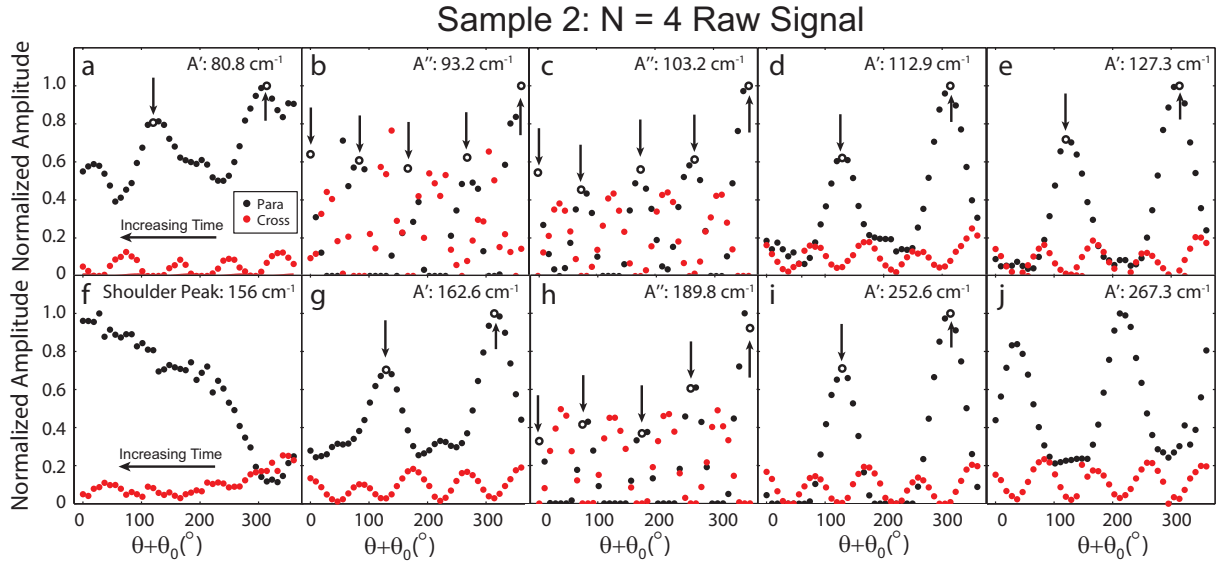


Figure S3: Raw normalized Raman amplitudes for parallel (red) and crossed (black) polarizations for the $N = 4$ and $N = 3$ region of Sample 2 from the main text. The symmetry and position for each mode are labeled. Signal decrease with time is attributed to laser damage.

normalized by its initial signal. The A_g/A' and B_g/A'' modes are shown in blue and red, respectively. These data were taken from the polarization dependence plots and therefore only the polarization angles that gave a maximum for each mode are shown. For these two different samples a similar signal decrease is observed and the empirical exponential fits are shown

as solid lines. Additional SHG images were taken afterwards and a decreased SHG signal in the damage area was observed. Figure S4 e shows an scanning electron microscopy (SEM) image of the sample in the main text and the laser damage sites are labeled. This shows that the $N = 4$ is still present, which suggests that the signal decrease is likely due to laser induced depletion of the tellurium.^{S13,S14} Note that no laser damage from SHG measurements was observed. This suggests that there is either less absorption for lower energy photons or the damage is due to heating, which is more significant for continuous wave lasers. Regardless of the mechanism, great care is required when taking Raman spectra of this material.

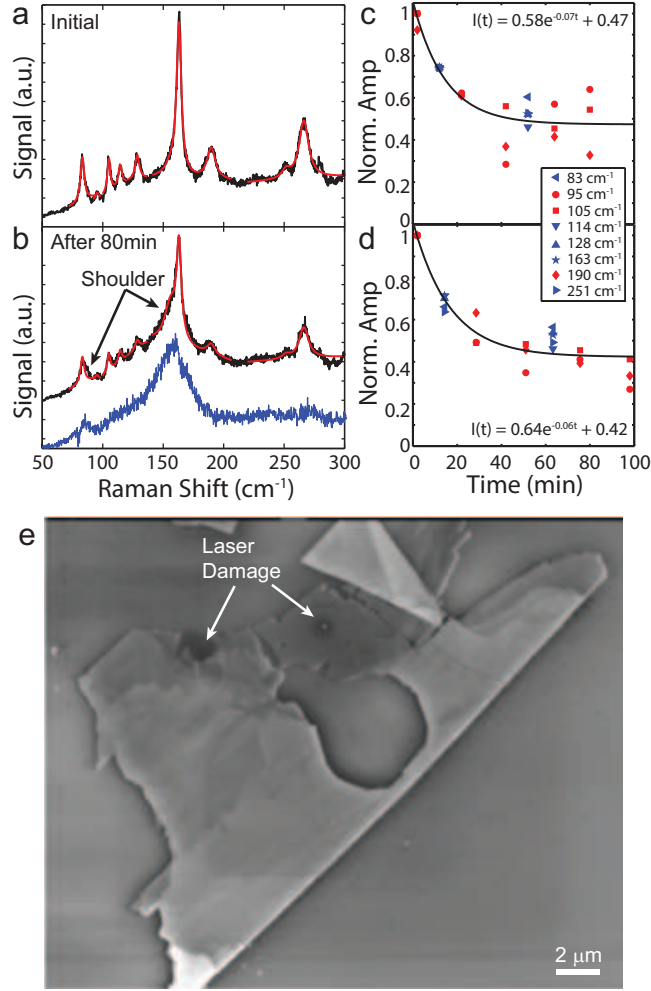


Figure S4: Raman spectra obtained during laser damage on $N = 4$ sample in Figure 1 d (a) initially and (b) after 80 min of laser exposure (black). Difference spectra of the initial and laser damaged spectra after scaling the amplitude is shown in blue to illustrate the shoulder peaks from the laser damage. (c),(d) Normalized amplitude of various Raman bands versus time for $N = 4$ sample in Figure 1 d and another $N = 4$ flake. (e) SEM image of sample in Figure 1 d after laser damage.

Sample orientation for SHG and Raman measurements

Figure S5(a),(b) shows the orientation of sample 2 on the SHG and Raman instrument, respectively. The dashed and solid white lines in Figure S5(a),(b) indicate the $[010]$ crystal plane (y axis), respectively. This shows that there is a $\approx -10^\circ$ angle difference in the sample mounting for the two measurements. Figure S5(c),(d) shows an SHG image and an optical image of sample 1 on the SHG and Raman instrument, respectively. The white

and black lines in Figure S5(a),(b) indicate the $[100]$ crystal plane (x axis), respectively. This shows that there is a $\approx -16^\circ$ angle difference in the sample mounting for the two measurements. The sample alignment for the two Raman images is almost identical with respect to the crystal axis, as expected from the polarized Raman measurements Figs. S2-S3.

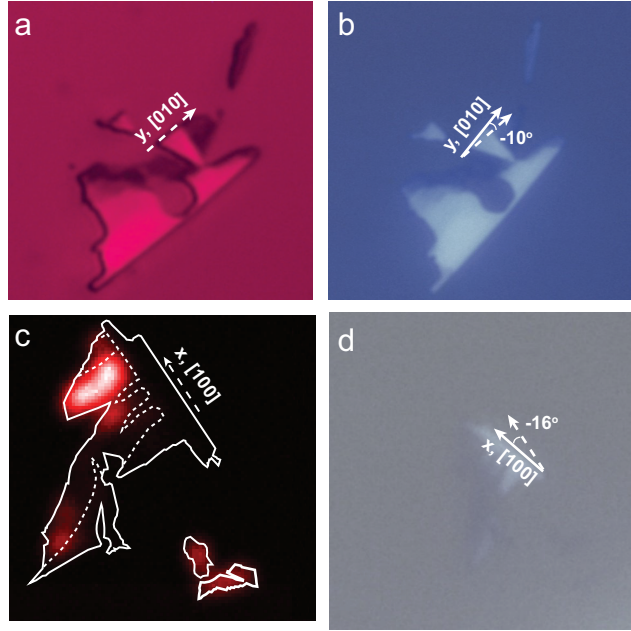


Figure S5: Optical image of sample 2 on the (a) SHG and (b) Raman instruments. The $[010]$ crystal plane (y axis) is labeled in dashed and solid white lines, respectively. The angle difference in the sample mounting of $\approx -10^\circ$ for the two measurements is indicated. (c) SHG and (d) optical images of sample 1. The $[100]$ crystal plane (x axis) is labeled in dashed and solid white lines, respectively. The angle difference in the sample mounting of $\approx -16^\circ$ for the two measurements is indicated.

Thickness verification using white light and Raman spectra

The thickness of the samples was verified using white light contrast and Raman spectra. The white light image of sample 1 from the main manuscript is shown in Figure S6 a. Linecuts along the 3L (red dashed line) and 4L (blue dashed line) for the blue, green, and red channels

of the camera are shown in Figure S6 b-d, respectively. The contrast was normalized using $(I - I_0)/I_0$. These cross sections show that contrast is better using green and red channels. The normalized contrast for the 4L region in the red and green channel is -0.4 and -0.3 in the green channel for the 3L region. The green channel indicates that the contrast is 33% higher for the 4L region in agreement with the AFM thickness measurements.

The thickness was also characterized using the Raman spectra. Figure S6 e shows the spectra of the $\approx 160 \text{ cm}^{-1}$ peak from the 3L (black) and 4L (red) regions. Generally the Raman signal scales with the volume of the sample. For two-dimensional materials, this means that the Raman signal should scale linearly with the number of layers. The ratio of the amplitudes and areas are 0.75 and 0.80, respectively, which is in good agreement with the AFM thickness assignments.

White light contrast for sample 2 are shown in Figure S7 a and the linecuts along the 4L (yellow line), 5L region (red line), and 6L (black line) are shown in Figure S7 b-d, respectively for the red and green camera channels. The laser damage from the Raman measurements is also labeled. The red channel for the 6L region does not have as much contrast as expected, which is likely due to the small size of the flake.

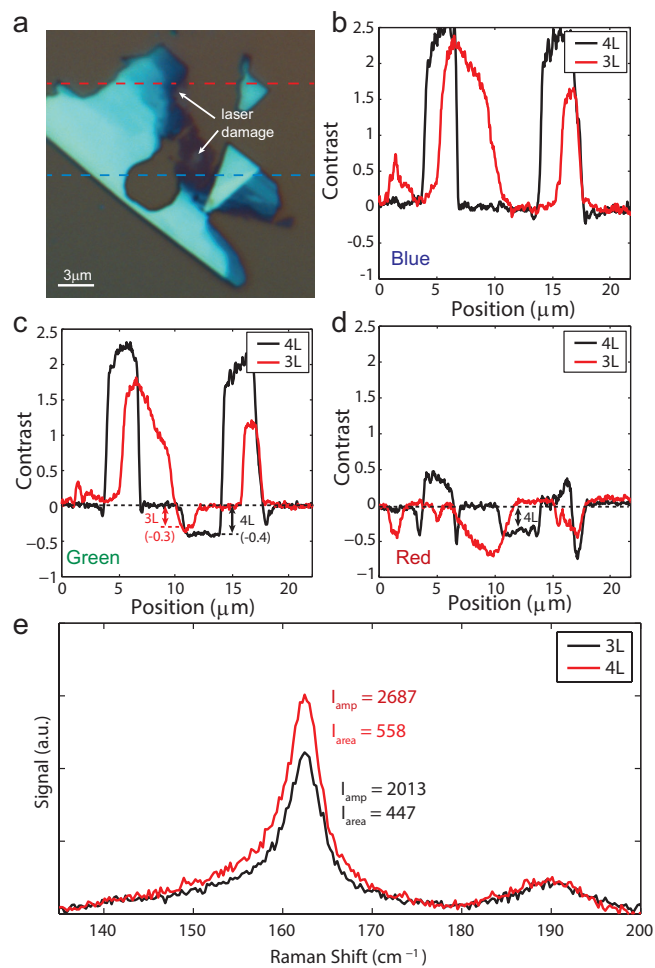


Figure S6: Sample thickness using white light contrast and Raman scattering (a) White light image of the flake taken using an RGB camera. The linecuts across the 3L (dashed red) and 4L (dashed blue) regions are shown. Linecuts from the (b) Blue, (c) green, and (d) red channels from the RGB camera with the 3L and 4L regions indicated. (e) Raman spectra of the $\approx 160 \text{ cm}^{-1}$ peak for the 3L and 4L regions. The area and amplitudes are labeled.

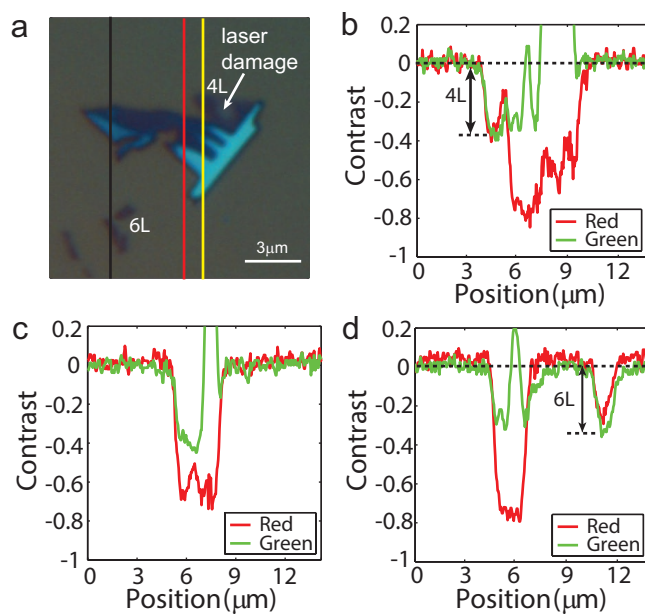


Figure S7: Sample thickness using white light contrast. (a) White light image of the flake taken using an RGB camera. The linecuts across the (b) 4L (yellow line), (c) 5L (red line), (d) 6L (black line) regions are shown. The green and red camera channels are shown.

SHG from additional flakes

Figure S8 show SHG measurements for four additional flakes with the thicknesses determined by AFM, white light, or both. The first column shows the SHG images with the topographic outlines and step edges shown as white lines. Figure S8 d-f shows a large 3L region with no SHG signal, whereas Figure S8 g-i shows strong SHG from the 4L region and the SHG image is in good agreement with the shape of the region from the white light region. Finally Figure S8 j-l shows a flake with a large number of step edges and the SHG image is again in good agreement with the step edges. These images provide additional evidence for the SHG only being present on thin even layer flakes.

Figure S9 shows the white light, topographic, and SHG images of the 10L crystal shown in green in Figure 4 f of the main text. The black square in Figure S9 a indicates the SHG scan area for Figure S9 c. Figure S9 b shows the topography with the 10L region near the bottom of the image.

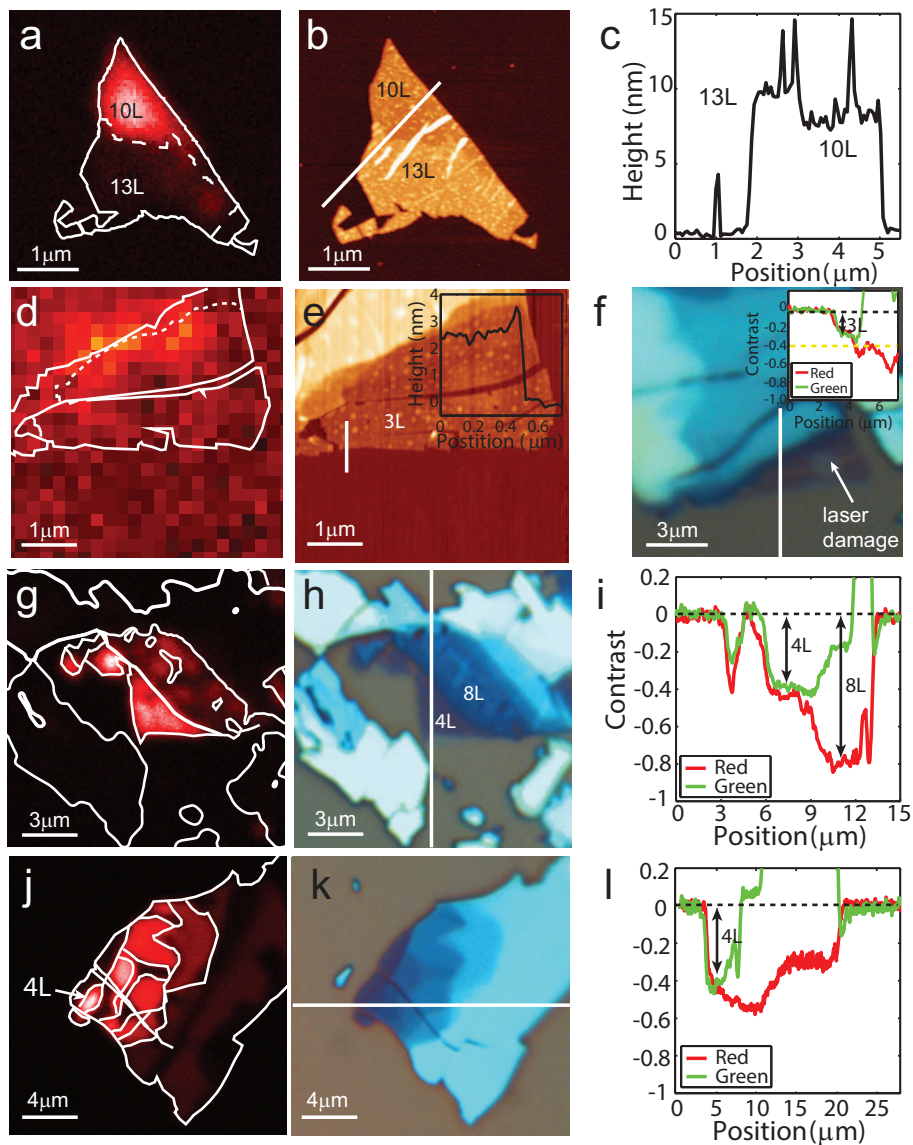


Figure S8: SHG images of additional flakes. First column shows the SHG images. The other two columns show AFM and white light images with linecuts to show the thicknesses. The red (red lines) and green (green lines) channels from the white light camera are shown.

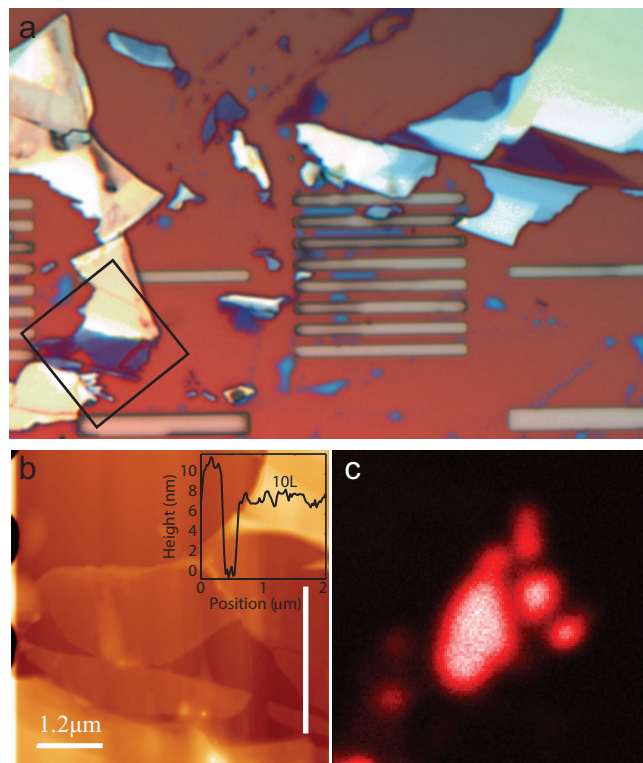


Figure S9: Images of the 10L crystal whose SHG polarization is shown in green in Figure 4 f of the main text. (a) White light image and the black square shows the SHG scan window. (b) Topography image with part of the 10L region shown near the bottom. (c) SHG image of the 10L region.

Topographic images

Figure S10 shows the AFM images for Figure 4 of the main text.

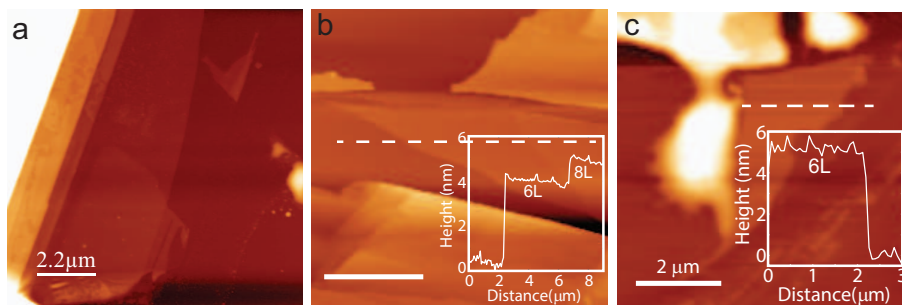


Figure S10: Topography of the regions in Figure 4 of the main text.

References

- (S1) Dresselhaus, M.; Dresselhaus, G.; Jorio, A. *Group Theory: Application to the Physics of Condensed Matter*; SpringerLink: Springer e-Books; Springer Berlin Heidelberg, 2007.
- (S2) Janisch, C.; Wang, Y.; Ma, D.; Mehta, N.; Elías, A. L.; Perea-López, N.; Terrones, M.; Crespi, V.; Liu, Z. Extraordinary Second Harmonic Generation in Tungsten Disulfide Monolayers. *Sci. Rep.* **2014**, *4*.
- (S3) Ribeiro-Soares, J.; Janisch, C.; Liu, Z.; Elías, A.; Dresselhaus, M.; Terrones, M.; Cançado, L.; Jorio, A. Second Harmonic Generation in WSe₂. *2D Mater.* **2015**, *2*, 045015.
- (S4) Kudryavtsev, A.; Lavrov, S.; Shestakova, A.; Kulyuk, L.; Mishina, E. Second Harmonic Generation in Nanoscale Films of Transition Metal Dichalcogenide: Accounting for Multipath Interference. *AIP Adv.* **2016**, *6*, 095306.
- (S5) Mouri, S.; Miyauchi, Y.; Matsuda, K. Tunable Photoluminescence of Monolayer MoS₂ via Chemical Doping. *Nano Lett.* **2013**, *13*, 5944–5948.
- (S6) Li, H.; Zhang, Q.; Yap, C. C. R.; Tay, B. K.; Edwin, T. H. T.; Olivier, A.; Bailargeat, D. From Bulk to Monolayer MoS₂: Evolution of Raman Scattering. *Adv. Funct. Mater.* **2012**, *22*, 1385–1390.
- (S7) Chen, B.; Sahin, H.; Suslu, A.; Ding, L.; Bertoni, M. I.; Peeters, F.; Tongay, S. Environmental Changes in MoTe₂ Excitonic Dynamics by Defects-Activated Molecular Interaction. *ACS Nano* **2015**, *9*, 5326–5332.
- (S8) Cho, S.; Kim, S.; Kim, J. H.; Zhao, J.; Seok, J.; Keum, D. H.; Baik, J.; Choe, D.-H.; Chang, K.; Suenaga, K.; Kim, S. W.; Lee, Y. H.; Yang, H. Phase Patterning for Ohmic Homojunction Contact in MoTe₂. *Science* **2015**, *349*, 625–628.

- (S9) Mirgorodsky, A.; Merle-Méjean, T.; Champarnaud, J.-C.; Thomas, P.; Frit, B. Dynamics and Structure of TeO₂ Polymorphs: Model Treatment of Paratellurite and Tellurite; Raman Scattering Evidence for New γ - and δ -Phases. *J. Phys. Chem. Solids* **2000**, *61*, 501–509.
- (S10) Kumari, L.; Ma, Y.-R.; Tsai, C.-C.; Lin, Y.-W.; Wu, S. Y.; Cheng, K.-W.; Liou, Y. X-Ray Diffraction and Raman Scattering Studies on Large-Area Array and Nanobranched Structure of 1D MoO₂ Nanorods. *Nanotechnology* **2007**, *18*, 115717.
- (S11) Camacho-López, M.; Escobar-Alarcón, L.; Picquart, M.; Arroyo, R.; Córdoba, G.; Haro-Poniatowski, E. Micro-Raman Study of the m-MoO₂ to α -MoO₃ Transformation Induced by CW-Laser Irradiation. *Opt. Mater.* **2011**, *33*, 480–484.
- (S12) Amirtharaj, P.; Pollak, F. H. Raman Scattering Study of the Properties and Removal of Excess Te on CdTe Surfaces. *Appl. Phys. Lett.* **1984**, *45*, 789–791.
- (S13) Clarke, R.; Marseglia, E.; Hughes, H. A Low-Temperature Structural Phase Transition in β -MoTe₂. *Philos. Mag. B* **1978**, *38*, 121–126.
- (S14) Song, S.; Keum, D. H.; Cho, S.; Perello, D.; Kim, Y.; Lee, Y. H. Room Temperature Semiconductor–Metal Transition of MoTe₂ Thin Films Engineered by Strain. *Nano Lett.* **2015**, *16*, 188–193.